



Breakup of planar liquid sheets injected at high speed in a quiescent gas environment

Mohan Ananth¹ and Mario F. Trujillo^{1,†}

¹Engine Research Center, Department of Mechanical Engineering, University of Wisconsin-Madison, Madison, WI 53706, USA

(Received 9 June 2023; revised 4 September 2023; accepted 3 October 2023)

Using a combination of mean flow spatial linear stability and two-dimensional volume-of-fluid (VoF) simulations, the physics governing the instability of high-speed liquid sheets being injected into a quiescent gas environment is studied. It is found that the gas shear layer thickness δ_G plays an influential role, where for values $\delta_G/H \lesssim 1/8$, the growth of sinuous and varicose modes is nearly indistinguishable. Here, H is the liquid sheet thickness. With larger values of δ_G/H , a second peak develops in the lower wavenumber region of the dispersion relation, and becomes increasingly dominant. This second peak corresponds to a large-scale sinuous mode, and its critical wavelength $\lambda_{crit,sinuous}$ is found to scale as $\lambda_{crit,sinuous}/H = 14.26(\delta_G/H)^{0.766}$. This scaling behaviour collapses onto a single curve for various combinations of the liquid-based Reynolds (Re_L) and Weber (We_L) numbers, provided that $\delta_G/H > O(10^{-1})$. For the varicose modes, the shape of the dispersion relation does not change with variations in δ_G/H , and the liquid shear layer thickness has an almost negligible influence on the growth of instabilities. Two-dimensional VoF simulations are employed to examine the validity of the linear stability assumptions. These simulations also show that the dominant sinuous mode remains active as the process transitions into the nonlinear regime, and that this mode is ultimately responsible for fragmenting the sheet. Based on an energy budget analysis, the most influential contributors to the growth of the sinuous mode are the gas Reynolds shear stress and the lateral working of pressure on the gas side.

Key words: aerosols/atomization, shear-flow instability, multiphase flow

1. Introduction

The current work is aimed at characterizing and understanding, via volume-of-fluid (VoF) simulations and spatial linear stability analysis, the nature of instability growth

† Email address for correspondence: mtrujillo@wisc.edu

for sheets being injected into a quiescent environment at high speeds comparable to the speeds corresponding to the atomization regime for realistic fuel nozzles (Lefebvre & McDonell 2017, p. 28). The type of understanding sought in this investigation is vital for the development of low-order models, particularly in light of new reduced carbon fuels entering the market (Folkson 2014). To isolate the physics of hydrodynamic breakup from complexities associated with injector internal flow (Wang *et al.* 2017), a planar liquid sheet configuration is considered.

Early work analysing the instability of liquid sheets moving in still air was presented by Squire (1953), utilizing an inviscid analysis where it was predicted that the flow is unstable if

$$We_L = \frac{\rho_L U_{inj}^2 H/2}{\sigma} > 1. \quad (1.1)$$

Here, the liquid density, injection velocity, sheet thickness and surface tension coefficient are respectively given by ρ_L , U_{inj} , H and σ . Similar inviscid treatment was reported by Hagerty & Shea (1955) and Rangel & Sirignano (1991) comparing varicose to sinuous modes growth.

A natural progression of the early inviscid treatment was the inclusion of viscosity in the liquid while the surrounding gas remains inviscid (Dombrowski & Johns 1963; Li & Tankin 1991). In the work of Li & Tankin (1991), it was found that two modes of instability exist, namely an aerodynamic and a viscosity-enhanced instability. This is in contrast to the purely inviscid case, where only the aerodynamic mode was predicted. A more recent comparison between viscous and inviscid instability has been provided by Boeck & Zaleski (2005), where the complete viscous treatment is used. This amounts to the solution of the Orr–Sommerfeld equation in both the gas and liquid phases, in conjunction with interfacial constraints enforcing continuity of horizontal and normal velocity, and balance of shear and normal stresses. It is shown that for atomization conditions, the perturbation growth for the viscous case can be substantially larger than for the inviscid case.

The question of convective versus absolute instability has been a common theme in the investigation of breakup. One of the first papers on the topic by Li (1993) considered a thin-moving plane liquid sheet employing a potential flow treatment. The methodology used corresponds to a spatial instability analysis, and it was reported that for sinuous mode, there is a critical Weber number equal to 1 below which pseudo-absolute instability exists and above which convective instability occurs. For the varicose mode, the instability was found to be always convective. Employing an Orr–Sommerfeld system with all interfacial conditions enforced, Teng, Lin & Chen (1997) identified a critical We_L of approximately 1 below which the flow is absolutely unstable and above which it is convectively unstable. The configuration employed corresponds to a vertical viscous liquid sheet sandwiched between two viscous gas regions bounded by walls. Similar findings are also reported by De Luca & Costa (1997) concerning the critical value of We_L being approximately 1 for sinuous modes. The conditions leading to convective or absolute instability have also been investigated by Juniper (2007) using an inviscid approach, where the set-up consists of a central fluid layer surrounded above and below by a second fluid. The results from this work show that the confinement of the three fluid layers plays a critical role in the type of instability that develops. In our work, our system is unconfined.

Considering a configuration of two planar fluid sheets where the bottom layer is liquid and the top layer is gas, Fuster *et al.* (2013) reported that for low dynamic pressure ratios M and small e/Δ_G , the instability is convective, but for large dynamic pressures it transitions to an absolute instability. The ratio M is defined as $M = \rho_G U_G^2 / \rho_L U_L^2$. The distance

between the liquid and gas streams is denoted as e , and Δ_G is the vorticity thickness given by $\Delta_G = (\Delta U)/(dU/dy|_{max})$, where ΔU is the velocity difference between the gas and liquid streams. Their analysis corresponds to spatial-temporal treatment. Employing a liquid jet surrounded by a parallel annular gas flow configuration, Delon, Cartellier & Matas (2018) cite two mechanisms that can cause absolute instability. The first is driven by surface tension and occurs if $We_{U_i} = \rho_L U_i^2 / (\sigma k_i^*) < 1$, and the second is affected by flow confinement if $We_{U_i} > 1$ and $M > 1$, where U_i is the interfacial velocity, and k_i^* is the largest spatial growth rate. In the present work, values for We_{U_i} range from 5035 to 6.81×10^8 with $M = 0$. Hence the relevant instability is expected to be convective in our work. The same conclusion is reached based on the $We_L > 1$ condition of Li (1993), Teng *et al.* (1997) and De Luca & Costa (1997). At any rate, VoF simulations are also used to confirm these expectations.

Over the last 20 years, much work has been devoted to the liquid sheet or jet breakup occurring under coflowing gas conditions (Dombrowski & Johns 1963; Marmottant & Villermaux 2004; Altimira *et al.* 2010; Tammisola *et al.* 2011; Fuster *et al.* 2013; Matas & Cartellier 2013; Odier *et al.* 2015; Matas, Delon & Cartellier 2018; Delon *et al.* 2018; Odier, Balarac & Corre 2018; Kumar & Sahu 2019; Jiang & Ling 2020; Singh *et al.* 2020; Jiang & Ling 2021). In the work of Marmottant & Villermaux (2004) and Matas & Cartellier (2013), the authors state that under these conditions, the breakup process occurs in two stages. At first, a primary instability develops aided by shear, leading to wave formation. This is followed by a second stage where the crest of these waves is exposed to an instability of the Rayleigh–Taylor type. The primary instability is set by the vorticity thickness Δ_G (Marmottant & Villermaux 2004; Matas & Cartellier 2013) or shear layer thickness (Tammisola *et al.* 2011). Under slower gas velocities, the primary and Rayleigh–Taylor instabilities do not fragment the jet completely, and under these conditions, a flapping instability develops (Matas & Cartellier 2013), whose wavelength is visually larger than the jet diameter (see figure 1 of Matas & Cartellier 2013). The authors suggest that the detachment of the coflowing gas from the liquid jet caused by the primary instability creates the perturbation that feeds into the development of the flapping instability. This idea that a sinuous mode evolving into a flapping instability is an amplification of the primary instability is also echoed in the work of Odier *et al.* (2018), who consider a liquid jet exposed to an annular high-speed gas stream.

At least two distinct points exist between the instability phenomena occurring under coflowing gas conditions and the present one, which arises under liquid injection into a quiescent gas environment. First, the augmentation of the primary instability caused by the detachment of the high-speed gas is absent in our case since the gas is stationary, and the flow motion comes primarily from the liquid side. Second, compared to the coflowing case, we show in the present work that the emergence of a large-scale sinuous mode is not simply an augmentation of the primary instability but rather the manifestation of a different mode altogether.

Large-scale instability modes being responsible for the breakup of a liquid sheet or jet under liquid injection in quiescent conditions have been documented in the literature. For instance, in the experimental work of Hoyt & Taylor (1977), who considered high Reynolds number water jets issuing into still air, the jet was characterized initially by the growth of relatively small-scale modes driven by a shear instability. Further downstream, a much larger-scale mode developed, fragmenting the jet. Similar experimental findings have also appeared in the work of Wu & Faeth (1995) and Crapper, Dombrowski & Pyott (1975). More recently, via VoF simulations, Deshpande, Gurjar & Trujillo (2015) have shown that

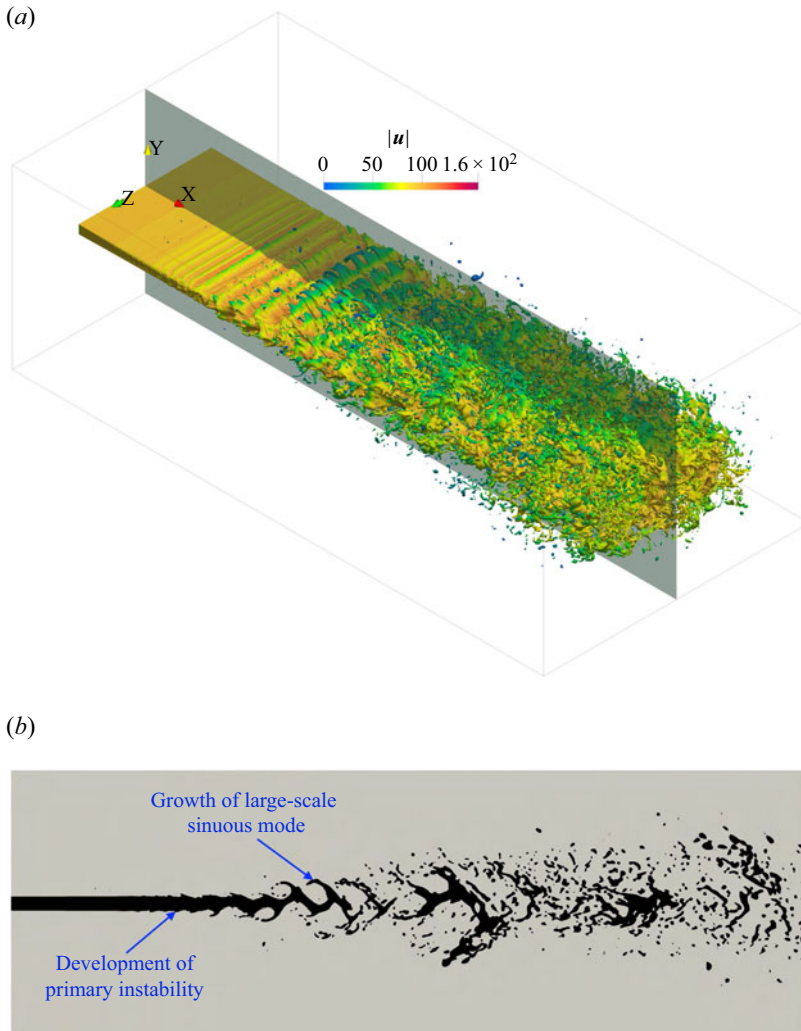


Figure 1. (a) Breakup of a liquid sheet injected into a stagnant air environment. (b) Side view of the development of the primary instability followed by the appearance of a large-scale sinuous mode. The inlet flow has a constant flat-hat profile without an imposed perturbation.

the fastest instability mode occurring at high-speed injection conditions is of such a small length scale that it is unable to displace the entire liquid core. Moving downstream, a much larger mode develops, breaking up the sheet. To illustrate this phenomenon more tangibly, VoF simulation results (described in § 4) of the sheet breakup under a stagnant environment are included in figure 1, which shows the development of the primary instability in the near field followed by the emergence of large-scale modes leading to the breakup of the sheet.

One of the aims of the present work is to analyse the conditions leading to the growth of these large-scale instabilities for liquid sheets injected into a still gas environment at high speed. To carry out this investigation, a spatial linear stability analysis is performed over a broad range of conditions, followed by VoF simulations. A key question is whether the dominant instability modes, which develop in the linear regime, continue to dominate as

the process becomes nonlinear. As elaborated previously, this process has been analysed well under coflowing conditions but has yet to receive the same level of attention under a quiescent gas environment. A second aim is to identify the critical contributors to the growth of the observed large-scale modes, which is done via an energy analysis of the perturbation.

The paper is organized as follows. First, the linear stability analysis (LSA) and the associated results are presented in §§ 2 and 3, respectively. This is followed by a description of the VoF methodology at the beginning of §4, an account of the VoF simulation set-up in § 4.1, the evaluation of LSA assumptions in § 4.2, and the comparison of VoF and LSA predictions in §§ 4.3 and 4.4. We then extend the analysis into the nonlinear regime via VoF in § 5, to determine the fate of the fastest growing modes. An energy budget analysis identifying the sources responsible for the amplification of instabilities is presented in § 6, followed by a summary and conclusions in § 7.

2. Linear stability treatment

Often in LSA of two-phase flows, the approach consists of solving for the evolution of a perturbation, which is superimposed on a base flow profile (Boeck & Zaleski 2005; Fuster *et al.* 2013; Matas *et al.* 2018). The adoption of this methodology can run into limitations when the base flow profile does not obey the governing equations exactly, but satisfies them only in an approximate sense. Additionally, for the types of problem considered here, which are motivated by fuel injection in engines and are therefore under high-speed conditions, it is not realistic to envision a base flow field that remains stable and steady. However, for much of the injection period, the flow fields in the near-field region of the injector nozzle are statistically stationary. Consequently, the mean fields within this statistically stationary or quasi-steady period can fulfil the role of the base flow field in LSA. It is in this spirit that we adopt a mean flow stability methodology in predicting the growth of disturbances. A detailed presentation of mean flow stability can be found in the works of Oberleithner, Rukes & Soria (2014) and Schmidt & Oberleithner (2020).

The configuration of interest consists of a planar liquid sheet of thickness H injected into a quiescent gas at speed U_{inj} . The governing equations for mass and momentum are given, respectively, by

$$\nabla \cdot \mathbf{u} = 0, \tag{2.1a}$$

$$\frac{\partial \mathbf{u}}{\partial t} + \mathbf{u} \cdot \nabla \mathbf{u} = -\frac{1}{\rho} \nabla p + \nu \nabla^2 \mathbf{u}. \tag{2.1b}$$

The density ρ , and the dynamic and kinematic viscosities μ and ν , are treated as constants in each thermodynamic phase. For the typical injection speeds and sheet thicknesses considered in the present work, Fr^2 is typically $O(10^5)$ or higher, thus gravitational effects can be ignored ($Fr = U_{inj}/\sqrt{gH}$, i.e. Froude number). Even if a length scale pertaining to the onset of breakup is used, the value for Fr^2 is still much greater than 1, making the gravitational effects negligible.

In the present adoption of mean flow LSA treatment, rather than imposing the triple flow decomposition of the flow field (Oberleithner *et al.* 2014; Schmidt & Oberleithner 2020), a Reynolds decomposition is used, where

$$\mathbf{u}(\mathbf{x}, t) = \bar{\mathbf{u}}(\mathbf{x}) + \mathbf{u}'(\mathbf{x}, t), \tag{2.2}$$

$$p(\mathbf{x}, t) = \bar{p}(\mathbf{x}, t) + p'(\mathbf{x}, t). \tag{2.3}$$

Here, the overline denotes the time average within the quasi-steady-state period of liquid injection, and the prime indicates the respective fluctuating quantity.

Averaging the governing equations yields

$$\nabla \cdot \bar{\mathbf{u}} = 0, \tag{2.4a}$$

$$\frac{\partial \bar{\mathbf{u}}}{\partial t} + \bar{\mathbf{u}} \cdot \nabla \bar{\mathbf{u}} + \nabla \cdot (\overline{\mathbf{u}'\mathbf{u}'}) = -\frac{\nabla \bar{p}}{\rho} + \nu \nabla^2 \bar{\mathbf{u}}, \tag{2.4b}$$

and by subtracting these two equations from (2.1), we obtain

$$\nabla \cdot (\mathbf{u}') = 0, \tag{2.5a}$$

$$\frac{\partial \mathbf{u}'}{\partial t} + \bar{\mathbf{u}} \cdot \nabla \mathbf{u}' + \mathbf{u}' \cdot \nabla \bar{\mathbf{u}} + \nabla \cdot (\mathbf{u}'\mathbf{u}' - \overline{\mathbf{u}'\mathbf{u}'}) = -\frac{\nabla p'}{\rho} + \nu \nabla^2 \mathbf{u}'. \tag{2.5b}$$

Adopting a two-dimensional (2-D) dimensionality with $\mathbf{u} = u(x, y, t) \mathbf{e}_x + v(x, y, t) \mathbf{e}_y$ and $p(x, y, t)$, where the streamwise, transverse and temporal coordinates are denoted by (x, y, t) , the momentum perturbation equation can be arranged as

$$\begin{aligned} \frac{\partial \mathbf{u}'}{\partial t} + \underbrace{\bar{u} \frac{\partial \mathbf{u}'}{\partial x} + v' \frac{\partial \bar{\mathbf{u}}}{\partial y}}_{\text{conventional advection}} + \underbrace{\bar{v} \frac{\partial \mathbf{u}'}{\partial y}}_{\text{transverse mean}} + \underbrace{\mathbf{u}' \frac{\partial \bar{\mathbf{u}}}{\partial x}}_{\text{streamwise developing}} \\ = -\frac{\nabla p'}{\rho} + \nu \nabla^2 \mathbf{u}' - \underbrace{\nabla \cdot (\mathbf{u}'\mathbf{u}' - \overline{\mathbf{u}'\mathbf{u}'})}_{\text{nonlinear}}. \end{aligned} \tag{2.6}$$

The conventional advection term is the one that is typically employed in the traditional linear stability treatments (Schmid & Henningson 2000; Criminale, Jackson & Joslin 2019). We assume that the transverse mean, streamwise developing and nonlinear terms are negligible. In § 4.2, it is shown that within a certain distance downstream of the inlet boundary, which depends on the type of instability considered, ignoring these additional advection terms is warranted. This space where these assumptions hold is referred to as the near-field region in the present work, where the LSA governing equations reduce to

$$\frac{\partial \mathbf{u}'}{\partial x} + \frac{\partial v'}{\partial y} = 0, \tag{2.7a}$$

$$\frac{\partial \mathbf{u}'}{\partial t} + \bar{u} \frac{\partial \mathbf{u}'}{\partial x} + v' \frac{d\bar{\mathbf{u}}}{dy} = -\frac{1}{\rho} \frac{\partial p'}{\partial x} + \nu \left(\frac{\partial^2}{\partial x^2} + \frac{\partial^2}{\partial y^2} \right) \mathbf{u}', \tag{2.7b}$$

$$\frac{\partial v'}{\partial t} + \bar{u} \frac{\partial v'}{\partial x} = -\frac{1}{\rho} \frac{\partial p'}{\partial y} + \nu \left(\frac{\partial^2}{\partial x^2} + \frac{\partial^2}{\partial y^2} \right) v'. \tag{2.7c}$$

It is understood implicitly that the field variables and physical properties take on values corresponding to the phase where they are being evaluated. For the mean flow fields, we impose the following profiles for $\bar{\mathbf{u}}$:

$$\bar{\mathbf{u}} = [\bar{u}, \bar{v}] = [\bar{u}(y), 0], \tag{2.8a}$$

$$\bar{u}_L(y) = -K_1 \operatorname{erf}\left(\frac{y - H/2}{\delta_L}\right) + K_2, \quad y \in [0, H/2], \tag{2.8b}$$

$$\bar{u}_G(y) = -K_2 \operatorname{erf}\left(\frac{y - H/2}{\delta_G}\right) + K_2, \quad y \in [H/2, W], \tag{2.8c}$$

Breakup of planar liquid sheets

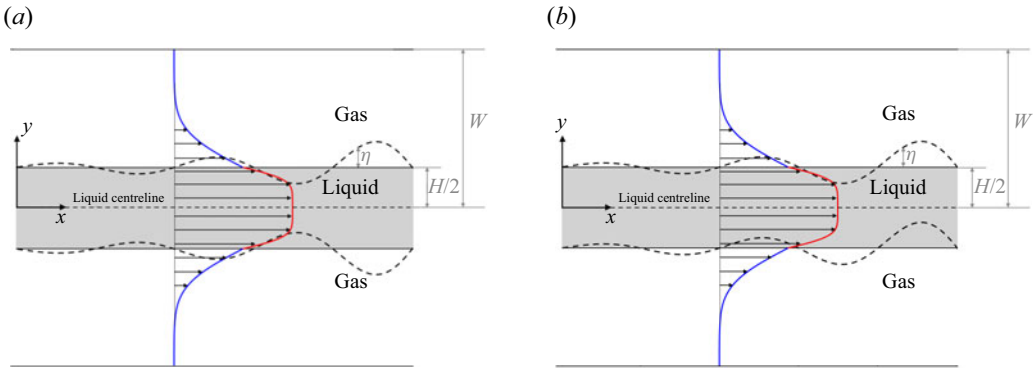


Figure 2. Schematic representation of the problem set-up, with (a) varicose perturbation and (b) sinuous perturbation. The flow is from left to right, and the nozzle orifice is located at $x = 0$.

where K_1 and K_2 are constants, δ is the shear layer thickness, and subscripts L and G indicate whether the quantity in question is liquid or gas. These error function profiles are used commonly in the literature (Yecko, Zaleski & Fullana 2002; Boeck & Zaleski 2005; Schmidt & Oberleithner 2020), and as explained in § 4.1, they are imposed at the inlet boundary of VoF simulations. The extent to which the VoF predictions of mean velocity retain their expected form (2.8) throughout the computational domain is evaluated in § 4.2. Furthermore, we also have the continuity of shear stress of the mean flow field at the mean interface location $y = H/2$:

$$\mu_L \left. \frac{d\bar{u}_L}{dy} \right|_{y=H/2} = \mu_G \left. \frac{d\bar{u}_G}{dy} \right|_{y=H/2}. \quad (2.9)$$

How sharp this mean interface location remains as we move downstream is also evaluated in § 4.2. Equations (2.8) substituted into (2.9) and $\bar{u}_L(y = 0) = U_{inj}$ yield

$$K_1 = \frac{U_{inj}}{1 + \frac{\delta_G \mu_L}{\delta_L \mu_G}}, \quad (2.10a)$$

$$K_2 = \frac{U_{inj}}{1 + \frac{\delta_L \mu_G}{\delta_G \mu_L}}, \quad (2.10b)$$

provided that $H/(2\delta_L) \gtrsim 3$.

As illustrated in figure 2, the governing equations for the perturbations (2.7) are solved in a half-domain with $y \in [0, W]$. By solving the problem in this fashion, the condition at the liquid centreline is varied depending on whether the perturbation mode is varicose or sinuous. Explicitly, the boundary conditions at the liquid centreline ($y = 0$) and at the gas boundary ($y = W$) are

$$\text{varicose} \quad \left[\frac{\partial u'_L}{\partial y} \right]_{y=0} = 0, \quad [v']_{y=0} = 0, \quad \left[\frac{\partial p'_L}{\partial y} \right]_{y=0} = 0; \quad (2.11a)$$

$$\text{sinuous} \quad [u'_L]_{y=0} = 0, \quad \left[\frac{\partial v'_L}{\partial y} \right]_{y=0} = 0, \quad [p'_L]_{y=0} = 0; \quad (2.11b)$$

$$\text{varicose and sinuous} \quad \left[\frac{\partial u'_G}{\partial y} \right]_{y=W} = 0, \quad [v'_G]_{y=W} = 0, \quad \left[\frac{\partial p'_G}{\partial y} \right]_{y=W} = 0. \quad (2.11c)$$

The second set of auxiliary conditions is imposed at the gas–liquid interface and constitutes the interfacial constraints given by

$$\left[-p'_G + 2\mu_G \frac{\partial v'_G}{\partial y} \right]_{y=H/2} - \left[-p'_L + 2\mu_L \frac{\partial v'_L}{\partial y} \right]_{y=H/2} = -\gamma \frac{\partial^2 \eta}{\partial x^2}, \quad (2.12a)$$

$$\mu_L \left[\frac{\partial u'_L}{\partial y} + \eta \frac{d^2 \bar{u}_L}{dy^2} + \frac{\partial v'_L}{\partial x} \right]_{y=H/2} = \mu_G \left[\frac{\partial u'_G}{\partial y} + \eta \frac{d^2 \bar{u}_G}{dy^2} + \frac{\partial v'_G}{\partial x} \right]_{y=H/2}, \quad (2.12b)$$

$$\left[\eta \frac{d\bar{u}_L}{dy} + u'_L \right]_{y=H/2} = \left[\eta \frac{d\bar{u}_G}{dy} + u'_G \right]_{y=H/2}, \quad (2.12c)$$

$$[v'_L]_{y=H/2} = [v'_G]_{y=H/2} \quad (2.12d)$$

and

$$\frac{D\eta}{Dt} = [v'_L]_{y=H/2}, \quad (2.12e)$$

where γ is the surface tension coefficient. Equations (2.12a) and (2.12b) represent the normal stress and shear stress balances. Continuity of horizontal and vertical velocities are given by (2.12c) and (2.12d). The interfacial displacement from the mean interfacial location ($y = H/2$) is given by $\eta(x, t)$, as shown in figure 2, and the kinematic condition is given by (2.12e).

To proceed with the calculation of perturbation growth rate, a normal mode decomposition is employed for treating the perturbations (Drazin & Reid 1981, p. 128):

$$[u'(x, y, t), v'(x, y, t), p'(x, y, t)] = [\hat{u}(y), \hat{v}(y), \hat{p}(y)] \exp[i(kx - \omega t)], \quad (2.13)$$

where $\hat{u}(y)$, $\hat{v}(y)$, $\hat{p}(y)$ are complex quantities, e.g. $\hat{u}(y) = \hat{u}_R(y) + i\hat{u}_I(y)$. For the kinematic condition, the method of characteristics combined with the normal mode form can be used to obtain

$$\eta(x, t) = \hat{\eta} \exp[i(kx - \omega t)], \quad \text{with } \hat{\eta} = \left[\frac{\hat{v}_{(L,G)}}{ikU_{(L,G)} - i\omega} \right]_{y=H/2}. \quad (2.14)$$

Since we are dealing with a spatial instability analysis, the frequency is given by $\omega = \omega_R \in \mathbb{R}$, and the wavenumber is given by $k = k_R + ik_I \in \mathbb{C}$. The components k_R and k_I represent the wavenumber and the spatial growth rate of the perturbation, respectively.

ρ_L (kg m ⁻³)	ρ_G (kg m ⁻³)	μ_L (Pa s)	μ_G (Pa s)	γ (N m ⁻¹)	
666.7	50	4.632×10^{-4}	1.88×10^{-5}	0.02	
H (μm)	W (μm)	U_{inj} (m s ⁻¹)	Re_L	We_L	Oh_L
90	900	100	12 955	15 000	0.0134

Table 1. Physical properties of fluids and key non-dimensional quantities used in LSA and VoF predictions, along with the nominal values for operating parameters.

The velocities and pressure are non-dimensionalized as

$$\tilde{U} = \frac{U}{U_{inj}}, \quad \tilde{u} = \frac{\hat{u}}{U_{inj}}, \quad \tilde{v} = \frac{\hat{v}}{U_{inj}}, \quad \tilde{p} = \frac{\hat{p}}{\rho_L U_{inj}^2}, \quad (2.15a-d)$$

and similarly, the non-dimensional wavenumber and frequency are given by, respectively,

$$\tilde{k} = kH, \quad \tilde{\omega} = \frac{\omega H}{U_{inj}}. \quad (2.16a,b)$$

In addition to the Weber number (1.1), two additional non-dimensional quantities appear in the analysis, namely the liquid-based Reynolds and Ohnesorge numbers,

$$Re_L = \frac{\rho_L U_{inj} H}{\mu_L} \quad \text{and} \quad Oh_L = \frac{\sqrt{2 We_L}}{Re_L}. \quad (2.17a,b)$$

The normal mode decomposition is substituted into the governing equations, boundary conditions and interfacial constraints, and a Chebyshev spectral representation is employed. The details of this procedure are included in the Appendix. The resulting final system that is solved is

$$\begin{bmatrix} -C_1 & -C_0 \\ I & \mathbf{0} \end{bmatrix} \cdot \begin{bmatrix} \tilde{k}a \\ a \end{bmatrix} - \tilde{k} \begin{bmatrix} C_2 & \mathbf{0} \\ \mathbf{0} & I \end{bmatrix} \cdot \begin{bmatrix} \tilde{k}a \\ a \end{bmatrix} = \mathbf{0}, \quad (2.18)$$

where the matrices C_0 , C_1 and C_2 are the coefficient matrices pertaining to the governing equations, boundary conditions and interfacial relations. The eigenvector and eigenvalue being solved for in this generalized eigenvalue problem are, respectively, $a = [a_u^L, a_v^L, a_p^L, a_u^G, a_v^G, a_p^G]^T$ and \tilde{k} .

3. Linear stability predictions

As reported in the works of Marmottant & Villermaux (2004), Fuster *et al.* (2013), Tammisola *et al.* (2011) and Matas & Cartellier (2013) under a coflow configuration, the size of the shear layer thickness has a profound effect on the type of instability that develops. Hence, in the present work, which considers injection in quiescent conditions, the impact of shear layer thickness is examined in the gas (δ_G) and liquid (δ_L) phases. The nominal conditions considered are presented in table 1. The size H is motivated by the orifice diameter of a commonly studied diesel type of injector, specifically the Engine Combustion Network Spray A nozzle (Engine Combustion Network, <https://ecn.sandia.gov/>). Some additional calculations have been performed (not shown) with different values

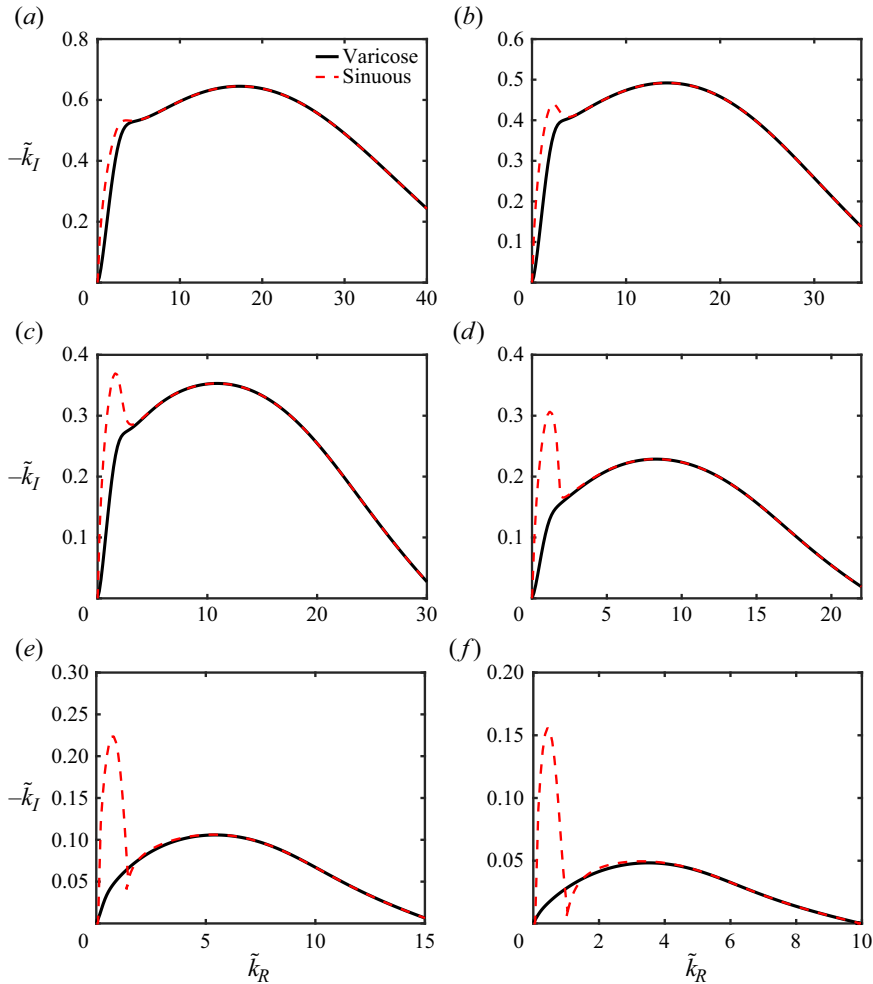


Figure 3. Spatial growth rate versus wavenumber for different gas shear layer thicknesses: (a) $\delta_G/H = 1/10$, (b) $\delta_G/H = 1/8$, (c) $\delta_G/H = 1/6$, (d) $\delta_G/H = 1/4$, (e) $\delta_G/H = 1/2$ and (f) $\delta_G/H = 1$. Conditions pertain to those listed in table 1. A new peak is observed at lower wavenumbers (higher wavelengths), which becomes dominant at $\delta_G/H = 1/6$.

of W to examine the containment effect. The results have shown that the results presented here are independent of W , provided that W is equal to at least $10H$.

First, predictions of spatial growth rate ($-k_I$) for both varicose and sinuous modes are plotted as a function of wavenumber, k_R , in figure 3. The six plots in the figure correspond to different values of δ_G/H , ranging from $1/10$ to 1 , while liquid shear layer thickness is held constant at $\delta_L = H/12$. At low values of δ_G/H , i.e. for $\delta_G/H \sim O(10^{-1})$, the peak in these dispersion curves is located at $k_R = kH \approx 15$, which implies that the length scale of the fastest growing mode is significantly smaller than H . As such, it is expected that these instabilities leave the inner core of the liquid sheet largely intact, and that their direct effect is a disruption limited to the sheet's surface. Beginning at approximately $\delta_G/H = 1/6$, a second peak develops at $k_R \approx 1$ for the sinuous mode. With larger values for the gas shear

Breakup of planar liquid sheets

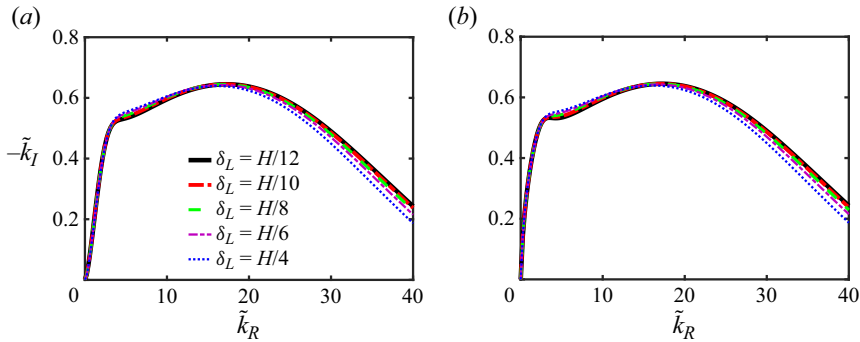


Figure 4. Spatial growth rate versus wavenumber for different liquid shear layer thicknesses corresponding to (a) varicose mode and (b) sinuous mode. Conditions pertain to those listed in table 1 with $\delta_G/H = 1/10$.

layer thickness, this second peak becomes progressively more dominant, and at $\delta_G/H = 1.0$, it is growing three times faster than the secondary peak.

The appearance of a dominant second peak with larger δ_G exists only for the sinuous mode. For the varicose mode, the fastest growing mode remains in the much larger wavenumber range. In fact, both sinuous and varicose mode predictions are almost indistinguishable, with the exception of the lower wavenumber range, i.e. $\tilde{k}_R \lesssim 2$. In this part of the wavenumber space, the sinuous growth rate deviates strongly from the varicose mode by manifesting much more significant growth. Since the associated length scale of this mode is comparable to or larger than H , its growth will lead ultimately to the total disruption of the sheet, provided that it survives beyond the linear regime. This behaviour is tested with the VoF simulations presented in § 5.

To examine the effect of δ_L , the previous calculations are repeated under the same conditions and fluid properties employed for the gas shear layer examination, but with δ_G fixed at $H/10$. The associated spatial growth rate curves are presented in figure 4, where δ_L/H ranges from $H/12$ to $H/4$. Unlike the previous predictions for the gas shear layer thickness, the growth rate curves remain almost the same as δ_L is varied for both varicose and sinuous modes. These results indicate that, at least within the linear regime of instability evolution, the liquid-based shear layer thickness has a negligible effect. Specifically, when we consider the fastest growing mode, the change in the corresponding wavenumber is less than 4% when δ_L is varied from $H/12$ to $H/4$.

The results shown in figure 4 lie in stark contrast to those presented by Turner *et al.* (2011), who report that the size of the shear layer in the denser fluid, i.e. the liquid, has the most significant effect on the growth rate of the disturbances. A closer look at the differences between their approach and the present work reveals that, most likely, the inviscid treatment (Rayleigh equation) and linear base profiles employed by Turner *et al.* (2011) are the contributing factors to the observed discrepancy. In our case, the viscous contribution is accounted for by the solution of the Orr–Sommerfeld system, along with the imposition of the full set of interfacial constraints. Compared to an inviscid treatment, the continuity of horizontal velocity and the shear stress condition are of particular significance. The argument made in Turner *et al.* (2011) is that with $Re_L \sim O(10^4)$, the viscous term can be neglected. While that may hold true for the base or mean velocities, the perturbation velocities have extremely sharp gradients at the interface (this is shown in a later section, specifically in figure 24); hence neglecting their associated viscous contribution is questionable.

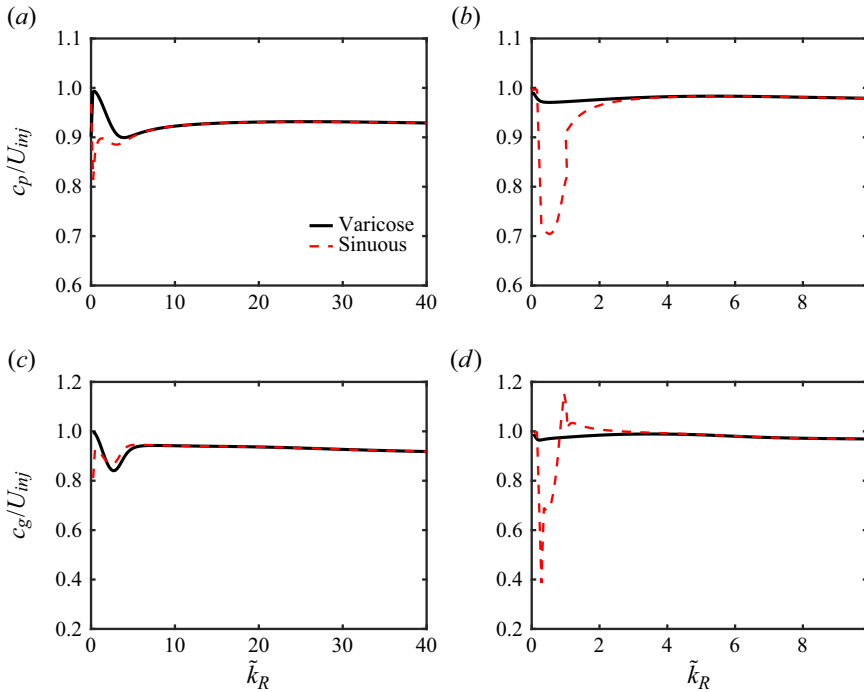


Figure 5. Phase velocities versus wavenumber for varicose and sinuous modes corresponding to (a) $\delta_G/H = 1/10$ and (b) $\delta_G/H = 1$. Group velocities versus wavenumber for varicose and sinuous modes corresponding to (c) $\delta_G/H = 1/10$ and (d) $\delta_G/H = 1$. Conditions pertain to those listed in table 1.

The associated phase velocities $c_p = U_{inj}\tilde{\omega}_R/\tilde{k}_R$ and group velocities $c_g = U_{inj} \partial\tilde{\omega}_R/\partial\tilde{k}_R$ are plotted in figure 5, corresponding to the two extreme values of δ_G/H , i.e. $\delta_G/H = 1/10$ and 1. Deviations of both c_p and c_g from the injection speed U_{inj} are noticeably more pronounced for low wavenumbers, and this deviation corresponds, for the most part, to a slower propagation of the disturbances. This effect is more significant for $\delta_G/H = 1$, and the wavenumber range where it occurs matches where the large-scale mode is detected for the sinuous mode. Indeed, it is the sinuous mode where the largest discrepancies from U_{inj} occur for the phase and group velocities. For the varicose mode at $\delta_G/H = 1$, all disturbances travel almost uniformly at U_{inj} . Even at $\delta_G/H = 1/10$, the varicose mode travels mostly with 10 % of the injection speed.

To examine whether the development of the large-scale sinuous mode occurs under a broader range of conditions, a number of additional cases are examined, as documented in table 2. The wavenumbers $k_{R,crit}$, corresponding to the critical or fastest growing mode for each of these cases, are extracted. The associated wavelengths $\lambda_{crit} (= 2\pi/k_{R,crit})$ are plotted in figure 6 for the sinuous mode, and in figure 7 for the varicose mode, as a function of the gas shear layer thickness. For the varicose case, $\lambda_{crit,varicose}/H$ increases monotonically with δ_G/H , i.e. $\lambda_{crit,varicose}/H \sim (\delta_G/H)^P$, where P varies between 0.54 to 0.64 for all curves.

In contrast, for the sinuous modes, beyond a value of δ_G/H ranging between 0.15 and 0.3, all curves collapse onto a single curve irrespective of Re_L and Oh_L , namely

$$\frac{\lambda_{crit,sinuous}}{H} = 14.26 \left(\frac{\delta_G}{H}\right)^{0.766}, \quad \delta_G/H \gtrsim 0.3. \tag{3.1}$$

Case number	Oh_L	U_{inj} (m s ⁻¹)	γ (N m ⁻¹)	Re_L
Case 1	0.013	50	0.02	6.477×10^3
Case 2		100		1.2955×10^4
Case 3		200		2.591×10^4
Case 4		300		3.8865×10^4
Case 5	0.066	20	0.0008	2.591×10^3
Case 6		50		6.477×10^3
Case 7		100		1.2955×10^4
Case 8		200		2.591×10^4
Case 9	0.13	300	0.0002	3.8865×10^4
Case 10		10		1.2955×10^3
Case 11		20		2.591×10^3
Case 12		50		6.477×10^3
Case 13	0.13	100	0.0002	1.2955×10^4
Case 14		200		2.591×10^4
Case 15		300		3.8865×10^4

Table 2. Additional high-speed injection cases examined under LSA. With the exception of a variable surface tension, the physical properties are the same as those listed in table 1.

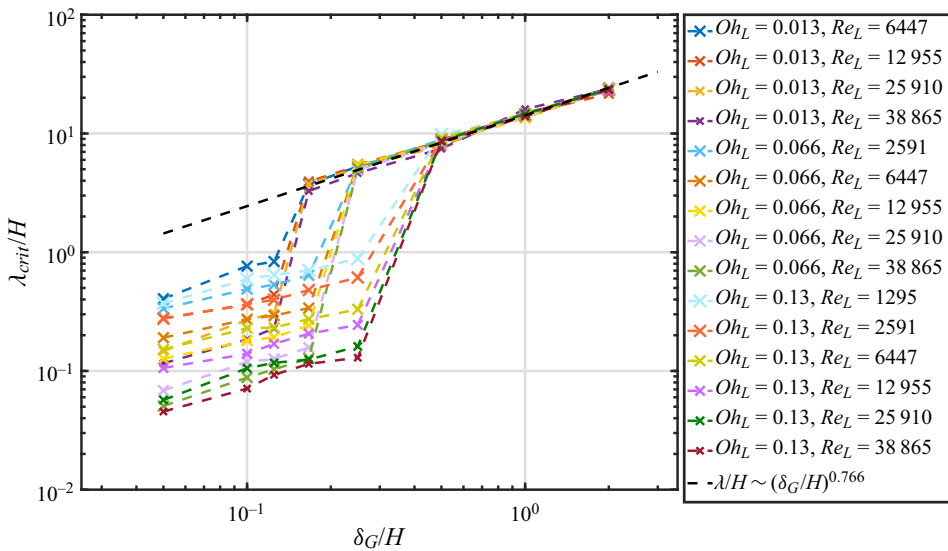


Figure 6. Predicted critical wavelengths from LSA corresponding to the sinuous mode.

This hints at a potential universality of the scaling of the critical wavelength with gas shear layer thickness for $\delta_G/H \gtrsim 0.3$. This collapse is accompanied by an abrupt change in the magnitude of $\lambda_{crit,sinuous}/H$, which increases by at least one order of magnitude as the maximum growth rate shifts from the high wavenumber region to the lower wavenumber range.

For smaller values of δ_G/H as shown in figure 6, i.e. $\delta_G/H \lesssim 0.1$, the critical sinuous mode wavelengths still scale with δ_G/H , i.e. $\lambda_{crit,sinuous}/H \sim (\delta_G/H)^P$, where P varies between 0.54 and 0.64. However, the collapse of all curves observed for $\delta_G/H \gtrsim 0.3$ is absent since each curve is distinct and varies depending on the associated

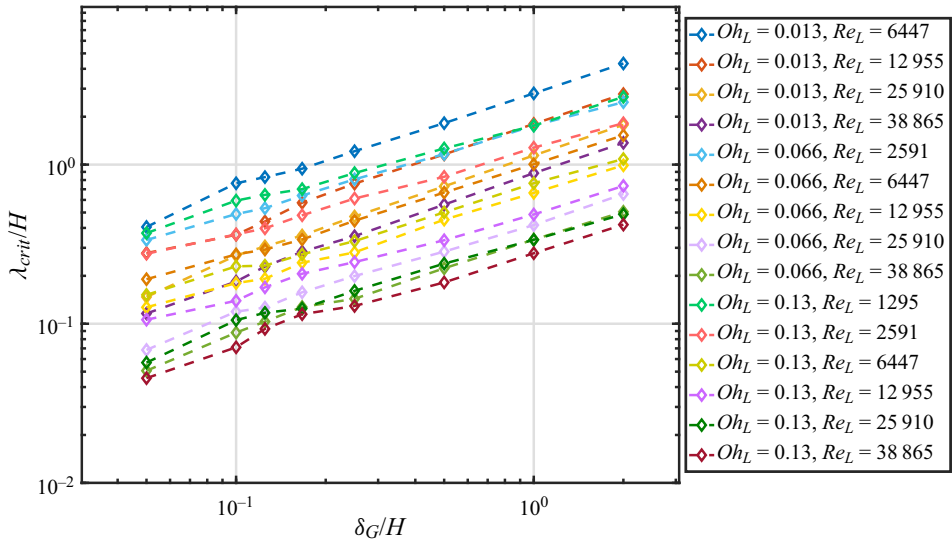


Figure 7. Predicted critical wavelengths from LSA corresponding to the varicose mode.

values for Re_L and Oh_L . Specifically, $\lambda_{crit, sinuous}/H$ decreases with increasing Re_L or increasing Oh_L . A transition region exists in the range $0.1 \lesssim \delta_G/H \lesssim 0.3$, where $\lambda_{crit}/H = f(\delta_G/H; Oh_L, Re_L)$ merges from a multi-valued function to practically a single-valued function with respect to the gas shear layer thickness.

To examine whether the dominant large-scale sinuous mode exists also at lower injection speeds, two additional cases are considered. The first is at $U_{inj} = 10 \text{ m s}^{-1}$ ($Re_L = 1295$ and $Oh_L = 0.013$), and the second is at $U_{inj} = 5 \text{ m s}^{-1}$ ($Re_L = 647$ and $Oh_L = 0.013$), with all fluid properties and H remaining the same. The resulting dispersion relations are plotted in figures 8 and 9 as functions of δ_G/H .

As opposed to the double-peak behaviour observed for $\delta_G/H \gtrsim 1/10$ (consider figure 3), the growth rates at these lower injection speed cases have a single peak. This implies that as the shear layer increases, the abrupt change in critical wavelength by one order of magnitude observed previously is absent under milder injection conditions. A second observation is that the range of wavenumbers where the growth rate is non-negligible is much smaller when compared to the growth rate curves under high-speed conditions. There are no peaks or even positive growth rates at high wavenumbers. In fact, $\lambda_{crit, sinuous}/H$ and $\lambda_{crit, varicose}/H$ are $O(1)$ for both lower velocity cases over the range of shear layer thickness considered.

4. Volume-of-fluid simulations

Capturing the full nonlinear dynamics of the perturbation process leading to the sheet breakup is done in the present investigation using a VoF methodology (Tryggvason, Scardovelli & Zaleski 2011). The particular flavour of the VoF method employed in the present study consists of an algebraic VoF solver phibasedFoam (Agarwal, Ananth & Trujillo 2022). This solver is a slightly modified version of the interFoam code, which is part of the OpenFoam open source distribution of continuum mechanics solvers (OpenFoam foundation, <https://openfoam.org/>). The discretization of the governing equations is done via finite volume. The solver begins with the evolution of α , which is

Breakup of planar liquid sheets

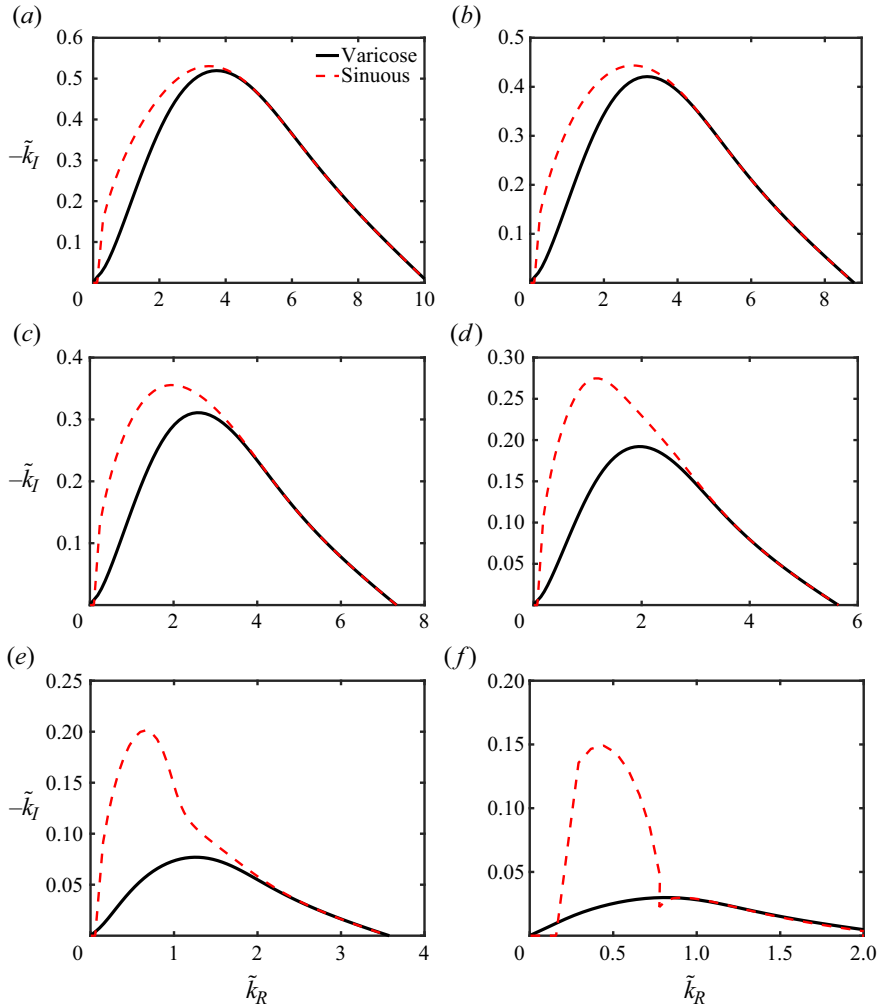


Figure 8. Spatial growth rate versus wavenumber for milder injection cases, for (a) $\delta_G/H = 1/10$, (b) $\delta_G/H = 1/8$, (c) $\delta_G/H = 1/6$, (d) $\delta_G/H = 1/4$, (e) $\delta_G/H = 1/2$, and (f) $\delta_G/H = 1$ (with $U_{inj} = 10 \text{ m s}^{-1}$, $Re_L = 1295$, $Oh_L = 0.0134$).

the fraction of liquid that occupies a given computational cell. This evolution is obtained from the solution of

$$\frac{\partial \alpha}{\partial t} + \nabla \cdot (\mathbf{u}\alpha) = 0. \quad (4.1)$$

To mitigate the effects of numerical diffusion of α due to its sharpness, the VoF scheme employs a compressive interface capturing methodology advanced by Ubbink & Issa (1999) and Rusche (2003), with contributions from Henry Weller. Subsequently, the following two-phase momentum equation is solved:

$$\frac{\partial(\rho \mathbf{u})}{\partial t} + \nabla \cdot (\rho \mathbf{u} \mathbf{u}) = -\nabla p + \nabla \cdot (\mu \nabla \mathbf{u}) + \nabla \mathbf{u} \cdot \nabla \mu + \rho \mathbf{g} + \sigma \kappa \nabla \alpha, \quad (4.2)$$

where the solenoidal condition of the velocity field has been used to expand the divergence of the stress tensor. The density and viscosity are obtained from $\rho = \rho_L \alpha + \rho_G(1 - \alpha)$ and

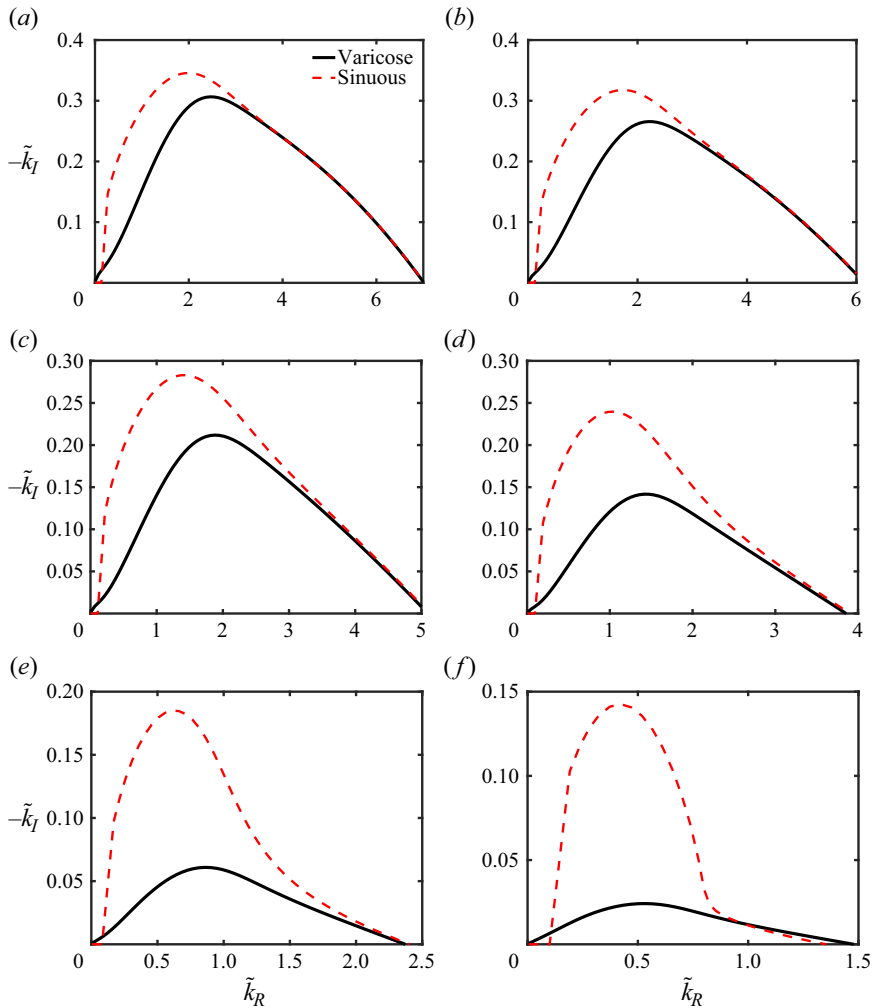


Figure 9. Spatial growth rate versus wavenumber for milder injection cases, for (a) $\delta_G/H = 1/10$, (b) $\delta_G/H = 1/8$, (c) $\delta_G/H = 1/6$, (d) $\delta_G/H = 1/4$, (e) $\delta_G/H = 1/2$ and (f) $\delta_G/H = 1$ (with $U_{inj} = 5 \text{ m s}^{-1}$, $Re_L = 647$, $Oh_L = 0.0134$).

$\mu = \mu_L \alpha + \mu_G (1 - \alpha)$ (Deshpande, Anumolu & Trujillo 2012). The last term on the right-hand side is the surface tension term based on the continuum surface force method (Brackbill, Kothe & Zemach 1992), where σ is the surface tension coefficient, and κ is the interface curvature defined as $\kappa = -\nabla \cdot [\mathbf{n}_\Gamma]$. Here, \mathbf{n}_Γ is the interface normal unit vector, given by $\mathbf{n}_\Gamma = \nabla \alpha / (|\nabla \alpha|)$. The prediction of velocity is followed by the solution of a pressure Poisson system with variable coefficients and a velocity corrector step. A description of the interFoam algorithm, along with an evaluation of its performance considering the various aspects of the two-phase flow solution, is provided in Deshpande *et al.* (2012).

A reported notable weakness in interFoam is the prediction of interfacial curvature, which is fundamental in the calculation of surface tension. To remedy this difficulty, phibasedFoam implements an improved curvature estimation by solving for a signed distance function ϕ_{dis} within the interfacial region coupled to the solution of the

Breakup of planar liquid sheets

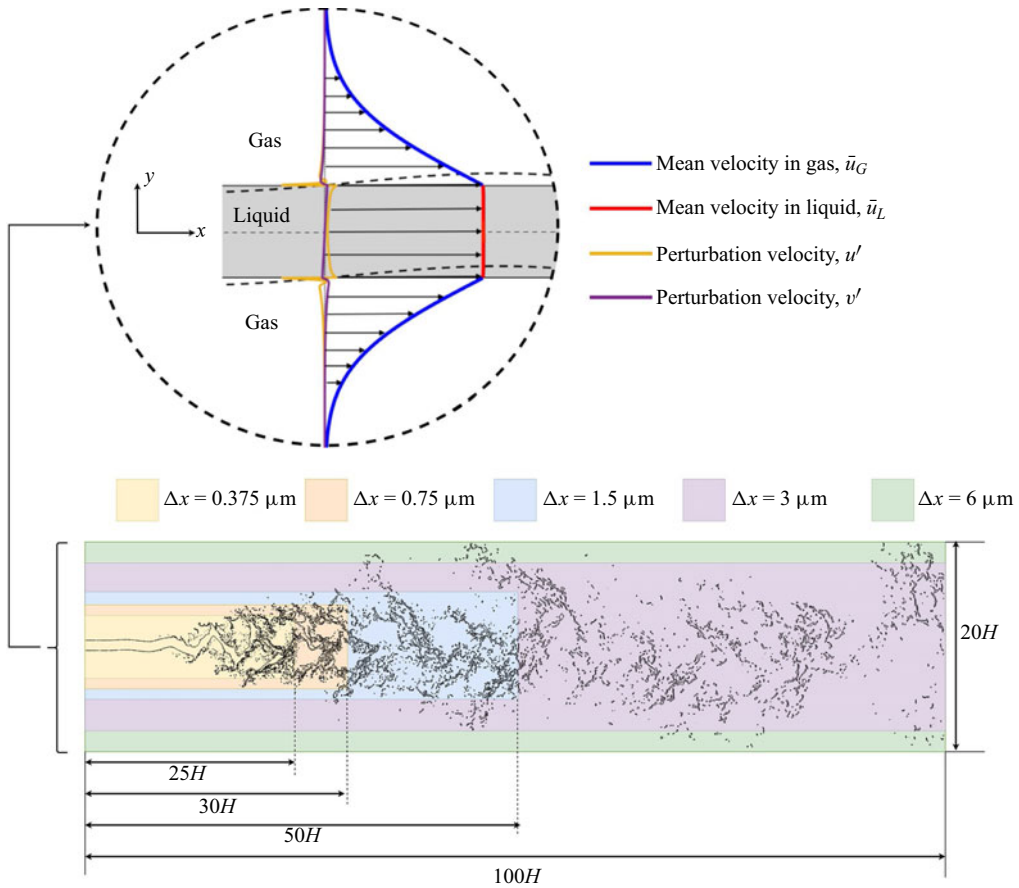


Figure 10. Depiction of the VoF domain employed in liquid sheet breakup simulations, along with the associated mesh resolution. The close-up view of the inlet provides details of the imposed velocity profile (4.6).

Hamilton–Jacobi equation away from this region. Based on this procedure, the predictions of curvature and the numerical convergence rate are improved noticeably. These improvements are much more substantial for cases that are either completely or heavily surface tension dominated. For the cases considered in the present work, which occur at much higher We_L values, we found that the differences were negligible in comparison to the standard interFoam.

4.1. Volume-of-fluid domain and initialization

Except for the calculations shown in figure 1, all the VoF computations presented in the paper are 2-D, allowing for much better resolution of the interfacial region. This is needed particularly for high-speed injection, where the perturbation eigenvectors become extremely sharp at the interface, requiring sub-micron resolution. Carrying out these calculations in three dimensions, where these perturbations are fully resolved numerically, poses a significant computational expense, especially in the calculation of statistical quantities, which require a sufficiently long time window. Additionally, since much of the focus of the work is on the initial development of instabilities, which are 2-D in nature, limiting the VoF simulations to two dimensions is reasonable.

The computational domain for the VoF calculation consists of a rectangular region having height $20H$ and length $100H$, as shown in [figure 10](#). This figure shows the varying levels of resolution Δx employed in different parts of the domain. Throughout the inlet region, grid size $\Delta x = 0.375 \mu\text{m}$ is used, which is sufficiently fine to resolve the perturbation velocities and perturbation pressure. As we move away from this region, the grid employed becomes progressively more coarse, and far away from the location of interest, the resolution is $\Delta x = 6 \mu\text{m}$.

The velocity profile imposed at the inlet is given by

$$u(x = 0, y, t) = \bar{u}(y) + u'(x = 0, y, t), \tag{4.3a}$$

$$v(x = 0, y, t) = v'(x = 0, y, t), \tag{4.3b}$$

where mean velocities are given in [\(2.8\)](#), and the perturbation velocities adopt a normal mode form [\(2.13\)](#), namely

$$u'(0, y, t) = \text{Re} \left[[\hat{u}_R(y) + i \hat{u}_I(y)] [\cos(kx - \omega_R t) + i \sin(kx - \omega_R t)] \right]_{x=0}, \tag{4.4}$$

$$v'(0, y, t) = \text{Re} \left[[\hat{v}_R(y) + i \hat{v}_I(y)] [\cos(kx - \omega_R t) + i \sin(kx - \omega_R t)] \right]_{x=0}. \tag{4.5}$$

Here, Re denotes the extraction of the real part of a complex expression. Substituting these expressions into [\(4.3\)](#) gives

$$u(x = 0, y, t) = \begin{cases} -K_1 \text{erf} \left(\frac{y - \frac{H}{2}}{\delta_L} \right) + K_2 + \hat{u}_{L,R}(y) \cos(\omega_R t) + \hat{u}_{L,I}(y) \sin(\omega_R t), & 0 < y < \frac{H}{2}, \\ -K_2 \text{erf} \left(\frac{y - \frac{H}{2}}{\delta_G} \right) + K_2 + \hat{u}_{G,R}(y) \cos(\omega_R t) + \hat{u}_{G,I}(y) \sin(\omega_R t), & \frac{H}{2} < y < W, \\ K_1 \text{erf} \left(\frac{y + \frac{H}{2}}{\delta_L} \right) + K_2 + \hat{u}_{L,R}(y) \cos(\omega_R t) + \hat{u}_{L,I}(y) \sin(\omega_R t), & -\frac{H}{2} < y < 0, \\ K_2 \text{erf} \left(\frac{y + \frac{H}{2}}{\delta_G} \right) + K_2 + \hat{u}_{G,R}(y) \cos(\omega_R t) + \hat{u}_{G,I}(y) \sin(\omega_R t), & -W < y < -\frac{H}{2}, \end{cases} \tag{4.6a}$$

$$v(x = 0, y, t) = \begin{cases} \hat{v}_{L,R}(y) \cos(\omega_R t) + \hat{v}_{L,I}(y) \sin(\omega_R t), & 0 < y < \frac{H}{2}, \\ \hat{v}_{G,R}(y) \cos(\omega_R t) + \hat{v}_{G,I}(y) \sin(\omega_R t), & \frac{H}{2} < y < W, \\ \hat{v}_{L,R}(y) \cos(\omega_R t) + \hat{v}_{L,I}(y) \sin(\omega_R t), & -\frac{H}{2} < y < 0, \\ \hat{v}_{G,R}(y) \cos(\omega_R t) + \hat{v}_{G,I}(y) \sin(\omega_R t), & -W < y < -\frac{H}{2}. \end{cases} \tag{4.6b}$$

The imposed perturbations at the inlet are ensured to be small by having the interfacial displacement $\hat{\eta}$, which is obtained from [\(2.14\)](#), to be 1.5 % of the liquid sheet thickness H .

Breakup of planar liquid sheets

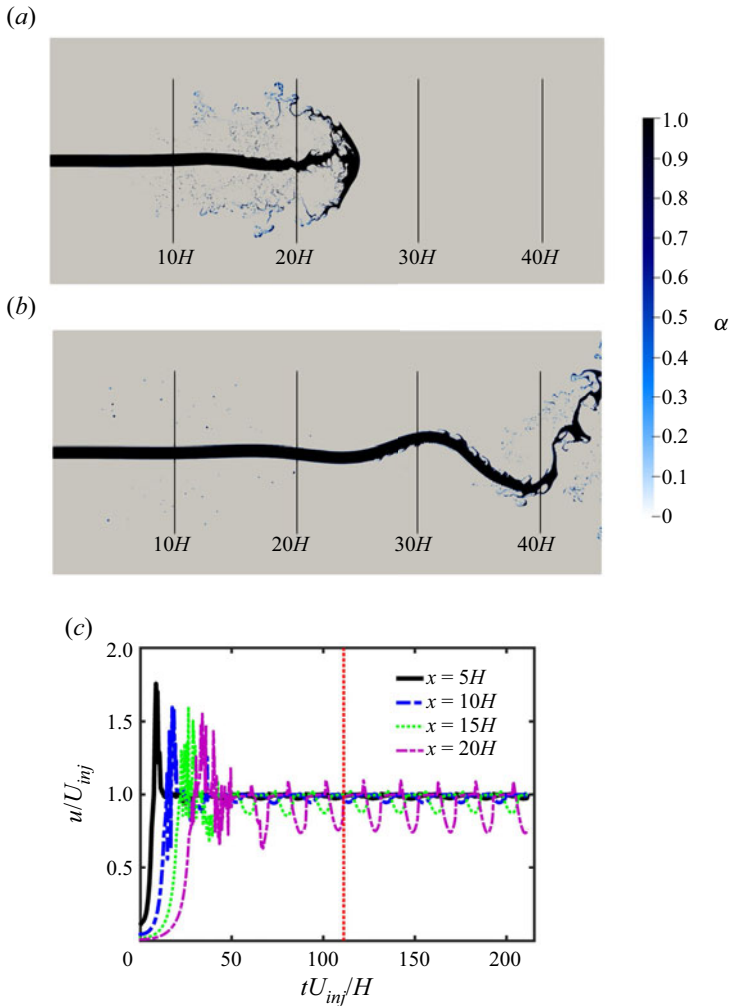


Figure 11. Example of a VoF simulation corresponding to the critical sinuous mode (table 1, $\tilde{\omega}_R = 0.3064$ and $\delta_G/H = 1$) at (a) $tU_{inj}/H = 33.33$, (b) $tU_{inj}/H = 222.22$, along with velocity time histories of probes located at various streamwise locations and at $y = H/2$.

The VoF simulations are initiated by imposing the velocity profiles of (4.6) on the inlet boundary as depicted in figure 10. This applies to both the liquid and gas phase portions of the inlet boundary. For example, a simulation of liquid sheet injection under conditions listed in table 1, and with a superimposed sinuous mode, is shown in figure 11. In figure 11(a), the sheet is captured during its initial injection period or initial transient, and in figure 11(b), the sheet resides within the quasi-steady-state period. Velocity time histories at various x locations and at $y = H/2$ are also shown in figure 11(c). These histories show that the initial transient caused by the passage of the sheet tip is recorded at progressively longer times with increasing distance from the inlet location. Beyond $tU_{inj}/H = 111$, as indicated by the red dashed line in figure 11(c), it is safe to assume that we have entered a quasi-steady state, and VoF data are collected only within this time period, i.e. not during the initial transient. This reference time $tU_{inj}/H = 111$ also holds for other excitation frequencies $\tilde{\omega}_R$ of the sinuous mode pertaining to the nominal conditions of table 1. Regarding the varicose mode, the physical domain of interest is much shorter,

as discussed in § 4.2. Therefore, the quasi-steady period is achieved more quickly, which implies that the reference initial time $tU_{inj}/H = 111$ is more than sufficient.

4.2. Validity of LSA assumptions

With the use of the VoF simulations, the various assumptions employed in the LSA can be examined. This entails the examination of both mean quantities as well as the various advection terms discarded in the perturbation equation (2.6). The VoF simulations are time-averaged from $tU_{inj}/H = 111$ to tU_{inj}/H ranging from 222.2 to 666.67, depending on the type of instability being considered. This comprises a sufficient time period to obtain statistically converged quantities within the domain $0 \leq x/H \leq 20$. Results corresponding to the sinuous and varicose modes are shown in figure 12. Both of these modes pertain to their respective critical condition, where the excitation frequency results in the peak growth rate predicted from linear stability. Here, the sinuous mode corresponds to $\delta_G/H = 1$, and the varicose mode to $\delta_G/H = 1/6$. This provides a sufficient range in the wavelengths of the perturbations observed.

Beginning with the streamwise mean velocity, the assumption made is that it conforms to an error function (2.8), and that this profile remains constant as we move downstream. Results shown in figure 12(a) confirm this behaviour, where \bar{u}/U_{inj} remains unchanged up to $x = 10H$, and begins to deviate slightly from the error function at $x = 15H$. Even at $x = 20H$, the profile retains its initial shape, but some slight smoothing takes place at approximately $y = \pm H/2$, i.e. the interfacial region. For the varicose mode, due to its much smaller wavelength, deviations from the error function profile happen sooner, as plotted in figure 12(b). Also, the deviations are concentrated in a narrower band around the interface, where the growth of small lumps is detected. Up to $x = 2H$, the mean streamwise velocity stays essentially unchanged, and this corresponds to approximately three wavelengths of the varicose mode. By $x = 4H$, there is a noticeable protrusion at the interface, while the rest of the velocity profile retains its original error function form. This means that predictions from LSA are likely to have difficulties for this mode beyond approximately $x = 4H$.

Regarding the transverse velocity, the time-averaged VoF data are shown in figure 12(c) for the sinuous mode and in figure 12(d) for the varicose mode. As given in (2.8), it is expected that both of these quantities should remain equal to zero. The results show that this was accomplished well for the sinuous mode up to $x = 20H$, with increasing levels of discrepancy with progressively longer distances from the inlet boundary. For the varicose mode, the approximation holds again in a much shorter range, and in comparison to the sinuous mode, the discrepancy is more significant. Nevertheless, its maximum value is approximately 2% of U_{inj} , which is still relatively small.

Finally, the mean liquid fraction fields are shown in figures 12(e) and 12(f) for the sinuous and varicose modes, respectively. Within the domain of interest, which extends up to $20H$ for the sinuous mode and $4H$ for the varicose mode, the varicose mode better retains its initial shape. Beyond $x = 10H$, the sinuous mode exhibits a noticeable degree of smoothing. This has an impact on the interfacial constraints in LSA, which are based on a departure η from the undisturbed interface location, i.e. $y = H/2$. Since beyond $x = 10H$ or worse, $x = 15H$, the interface is diffused over a larger band around $y = H/2$, and this implies a higher level of uncertainty in identifying the interface location, which is expected to have consequences in the calculation of interfacial constraints. However, below $x = 10H$, the degree of interface diffusion is relatively mild, and the interfacial region is sharp.

Breakup of planar liquid sheets

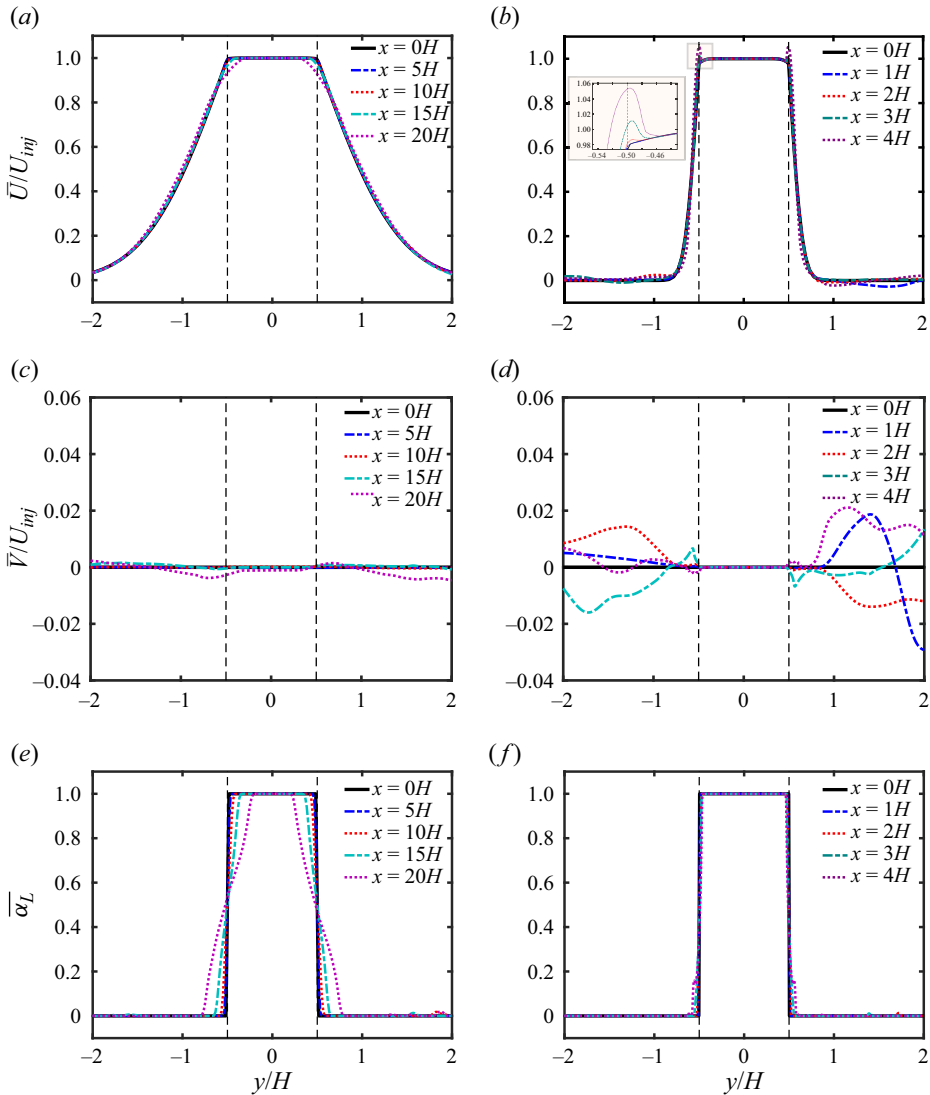


Figure 12. Average streamwise velocity for (a) the sinusoidal mode and (b) the varicose mode; average transverse velocity for (c) the sinusoidal mode and (d) the varicose mode; and average liquid fraction profiles for (e) the sinusoidal mode and (f) the varicose modes. The sinusoidal and varicose mode calculations correspond to their critical quantities, and the associated gas shear layer thicknesses used in the calculations are respectively $\delta_G/H = 1$ and $\delta_G/H = 1/6$. The operating parameters are those listed in table 1.

In conclusion, the findings depicted in figure 12 concerning mean quantities show that the assumptions inherent in LSA are valid for the sinusoidal mode up to $x = 10H$ or even perhaps $x = 15H$ for $\delta_G/H = 1$, while for the varicose mode, the domain of validity extends up to approximately $x = 3H$ for $\delta_G/H = 1/6$. In a more general sense, considering the ranges in δ_G/H employed in the present work, the range of validity is approximately $x = 6H$ to $x = 15H$ for the sinusoidal mode, and $x = 2H$ to $x = 15H$ for the varicose mode.

Turning our attention to the discarded terms in the perturbation evolution equation (2.6), we have the transverse mean, streamwise developing and the nonlinear term. Via VoF calculations, we can calculate these neglected terms and compare their magnitudes to the

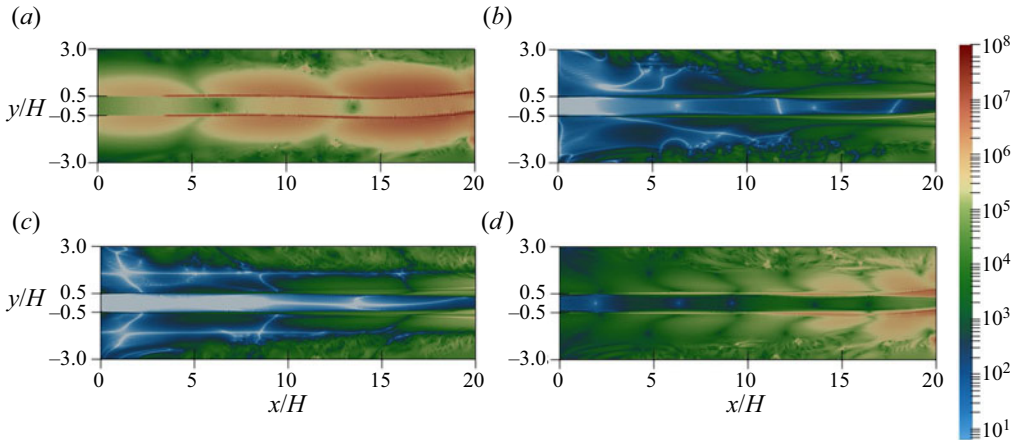


Figure 13. Instantaneous image plots at $tU_{inj}/H = 666.66$ of the various advection terms (absolute values) in the near field for the critical sinuous mode with $\delta_G/H = 1$ under conditions listed in [table 1](#): (a) $|\bar{u} \partial u' / \partial x + v' \partial \bar{u} / \partial y|$, (b) $|\bar{v} \partial u' / \partial y|$, (c) $|u' \partial \bar{u} / \partial x|$, (d) $|\nabla \cdot (\mathbf{u}' \mathbf{u}' - \overline{\mathbf{u}' \mathbf{u}'})|$.

magnitude of the retained conventional advection term. If these discarded terms can be shown to have a much lower magnitude than the conventional term over some range in x/H , then their omission is justified.

To get a sense of the magnitude and the general structure of each of the advection terms, image plots of their instantaneous values within the near-field region are shown in [figures 13](#) and [14](#) for the sinuous and varicose modes, respectively. A log scale is used to indicate their magnitude. First, the conventional term is significantly higher by orders of magnitude than the streamwise developing and transverse mean advection. It is actually the nonlinear contribution that competes more closely with the conventional advection term, but even this nonlinearity is at least an order of magnitude smaller. The results also show that the largest magnitude is concentrated in the interfacial region. Away from this region, there are errant droplets, which are remnants of the initial transient, that give the advection fields some degree of structure. This is apparent mostly for $|y| \gtrsim 2H$. Regarding the varicose mode, the same observation holds, with the exception that the shape of the interface is understandably different.

To gain a quantitative evaluation of the magnitude of the advection terms, a time average is taken of their absolute value as a function of x/H at $y = H/2$. As noted previously, this coincides with the undisturbed interface location. Since the advection terms pertain to fluctuating quantities, the absolute value is used in the time average. Otherwise, the time average naturally leads to progressively smaller values tending towards zero as the averaging period increases. The results are shown in [figure 15](#) for both critical sinuous and varicose modes.

For the sinuous mode, shown in [figure 15\(a\)](#), the conventional advection term is two to three orders of magnitude larger than their counterpart transverse mean and streamwise developing terms. The nonlinear term more closely approaches the magnitude of the conventional term, and the gap between these two decreases with increasing x/H as the nonlinearities grow in strength. For the varicose mode shown in [figure 15\(b\)](#), the difference between the conventional advection term and its counterparts is even larger, being approximately two to four orders of magnitude. Again, the nonlinear term is the largest discarded term, and the gap between it and the conventional term lessens as we move downstream from the inlet boundary. In summary, the assumption of only retaining

Breakup of planar liquid sheets

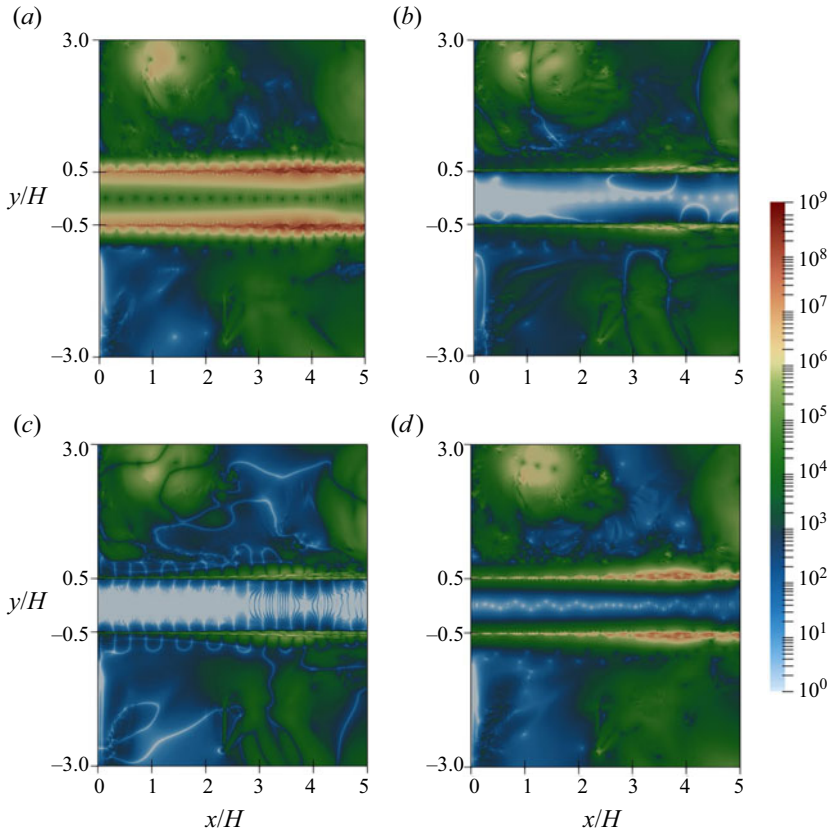


Figure 14. Instantaneous image plots at $tU_{inj}/H = 555.55$ of the various advection terms (absolute values) in the near field for the critical varicose mode with $\delta_G/H = 1/6$ under conditions listed in [table 1](#): (a) $|\bar{u} \partial u' / \partial x + v' \partial \bar{u} / \partial y|$, (b) $|\bar{v} \partial u' / \partial y|$, (c) $|u' \partial \bar{u} / \partial x|$, (d) $|\nabla \cdot (\mathbf{u}' \mathbf{u}' - \overline{\mathbf{u}' \mathbf{u}'})|$.

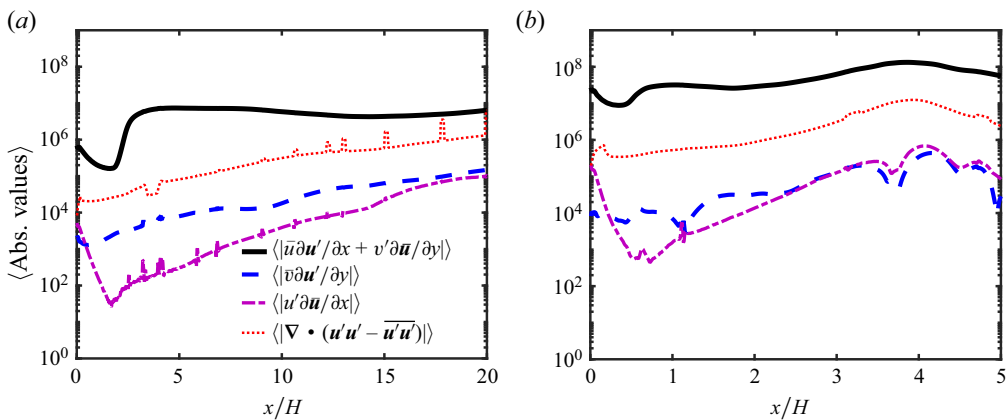


Figure 15. Time average of the absolute value of the various advection terms calculated under conditions listed in [table 1](#): (a) terms corresponding to the critical sinuous mode with $\delta_G/H = 1$; (b) terms corresponding to the critical varicose mode with $\delta_G/H = 1/6$.

the conventional advection term within the near field is warranted by the results from VoF simulations.

4.3. Extracting growth rates from VoF

To compare VoF and LSA predictions, perturbation growth rates are employed. Our approach for calculating these growth rates from VoF simulations is based on a procedure presented by Schmidt & Oberleithner (2020). It employs the kinematic relationship (2.12e), which is used to link the interface displacement with the normal perturbation velocity, namely,

$$\eta(x, t) = \frac{v'_L(x, y = H/2, t)}{i(k U_L(y = H/2) - \omega)}. \quad (4.7)$$

The disturbed normal velocity is obtained in the VoF simulations by probing it at the undisturbed location $(x, y = H/2)$. The time series of $v'(x, H/2, t)$ can be Fourier decomposed as

$$v'(x, H/2, t) = \sum_{n \neq 0} A_n(x, y = H/2) \exp(i\omega_n t), \quad (4.8)$$

where ω_n is the frequency of the n th Fourier mode and A_n is the corresponding amplitude. In the calculation of growth rate, only the fundamental mode ($n = 1$) is considered, and the extraction of $v'(x, H/2, t)$ data is extended only within a relatively small distance in the x direction, guaranteeing that the presence of other modes is negligible. Employing the normal mode decomposition, we have

$$v'(x, H/2, t) = \hat{v}(H/2) \exp(-k_I x) \exp[i(k_R x - \omega t)], \quad (4.9)$$

where $k = k_R + ik_I$. Considering only the fundamental mode and only the amplitude of both previous equations yields

$$A_1(x, y = H/2) = \hat{v}(H/2) \exp(-k_I x). \quad (4.10)$$

This can be repeated at some other position downstream of x ; for instance,

$$A_1(x + \Delta x, y = H/2) = \hat{v}(H/2) \exp(-k_I [x + \Delta x]). \quad (4.11)$$

Taking the ratio of both equations above, and taking the limit as $\Delta x \rightarrow 0$, we obtain

$$-k_I = \lim_{\Delta x \rightarrow 0} \left[\frac{\ln A_1(x + \Delta x, y = H/2) - \ln A_1(x, y = H/2)}{\Delta x} \right] = \frac{d}{dx}(\ln(A_1)), \quad (4.12)$$

which is the expression employed in the calculation of growth rate $-k_I$ from VoF data.

4.4. Comparison between linear stability and VoF

An examination of whether the predictions originating from the spatial LSA agree with the full Navier–Stokes treatment provided by the VoF is presented in this subsection. The nominal conditions pertaining to table 1 are chosen. Other VoF calculations performed at $Re_L = 25\,910$ and $Oh_L = 0.066$ have led to a similar agreement with LSA predictions but are excluded here for the sake of brevity. We consider two cases corresponding to the critical sinuous and varicose modes, and examine their behaviour as a function of gas shear layer thickness. The VoF calculations employ the inlet flow conditions described in (4.6), and the data are obtained in the quasi-steady-state period, as commented earlier.

Breakup of planar liquid sheets

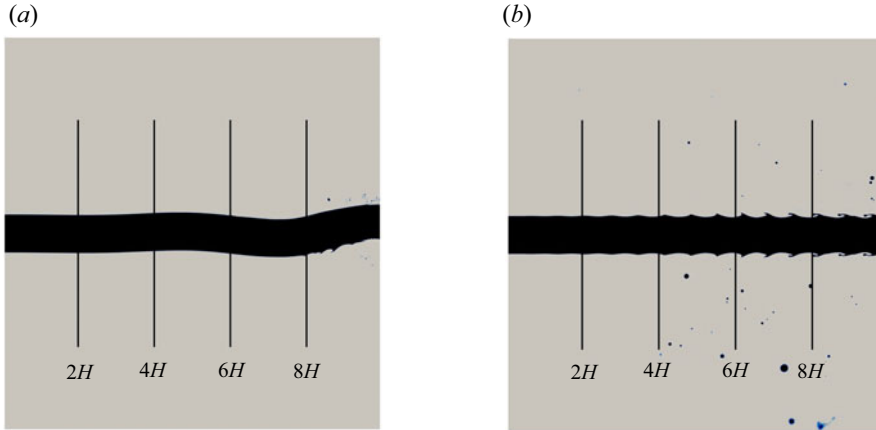


Figure 16. VoF simulation results for $\delta_G/H = 1/4$ corresponding to the critical (a) sinuous mode and (b) varicose mode. The distance from the inlet is displayed in terms of liquid sheet thickness H .

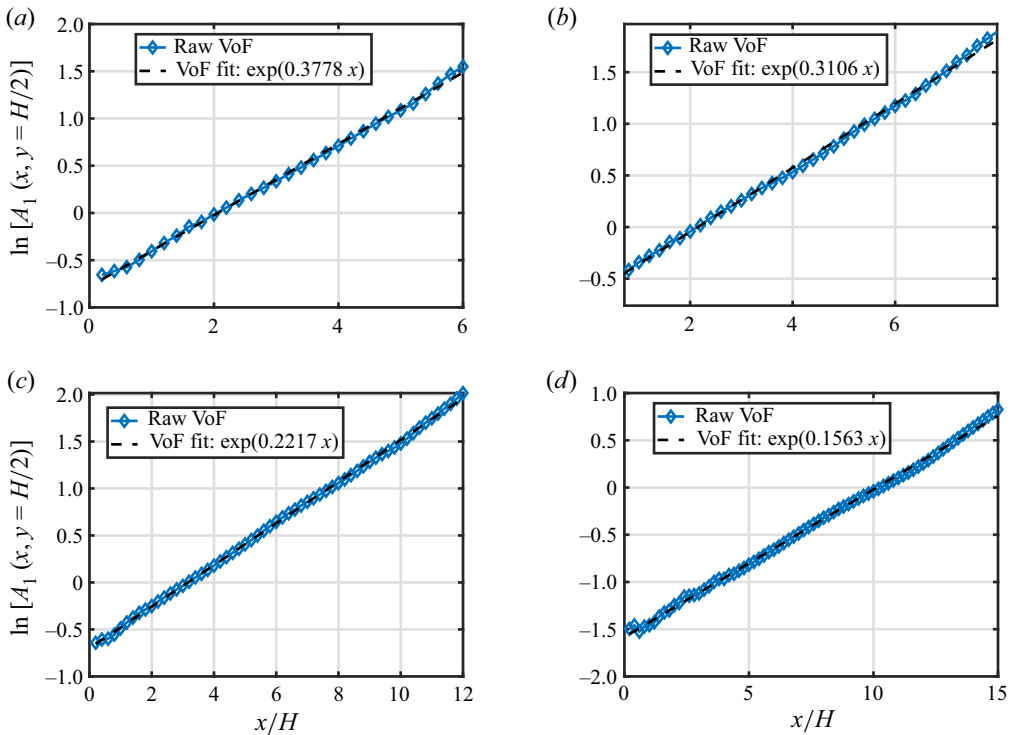


Figure 17. The VoF data corresponding to sinuous mode simulations and associated exponential curve fits (VoF fit). The respective values for gas shear layer thickness (δ_G/H) and growth rate predictions from LSA are: (a) $\delta_G/H = 1/6$, $-\tilde{k}_{I,LSA} = 0.3695$; (b) $\delta_G/H = 1/4$, $-\tilde{k}_{I,LSA} = 0.3053$; (c) $\delta_G/H = 1/2$, $-\tilde{k}_{I,LSA} = 0.2237$; (d) $\delta_G/H = 1$, $-\tilde{k}_{I,LSA} = 0.1559$.

Example VoF results are shown in [figure 16](#) for both modes, where a notable difference in perturbation length scale is clearly apparent. The sinuous mode has a wavelength that is approximately an order of magnitude longer than the varicose mode. In addition, some degree of surface breakup is observed for both cases towards the outflow face of the observation window as the perturbation grows.

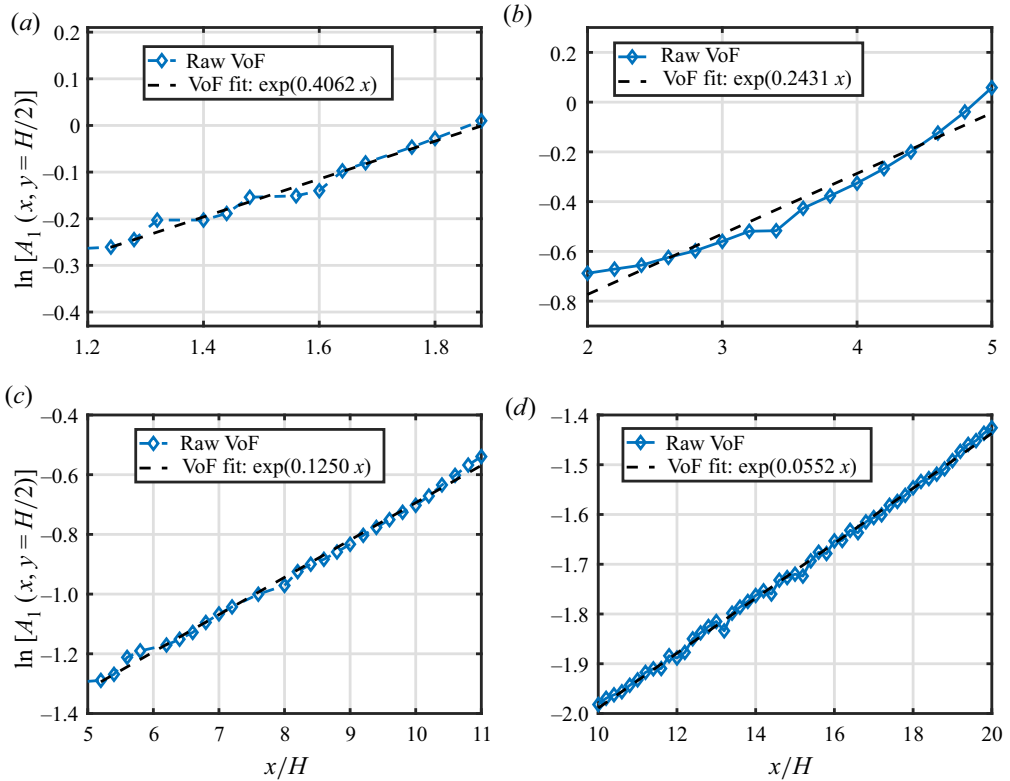


Figure 18. The VoF data corresponding to varicose mode simulations and associated exponential curve fits (VoF fit). The corresponding values of gas shear layer thickness (δ_G/H) and growth rate predictions from LSA are: (a) $\delta_G/H = 1/6$, $-\bar{k}_{l,LSA} = 0.3565$; (b) $\delta_G/H = 1/4$, $-\bar{k}_{l,LSA} = 0.2287$; (c) $\delta_G/H = 1/2$, $-\bar{k}_{l,LSA} = 0.1061$; (d) $\delta_G/H = 1$, $-\bar{k}_{l,LSA} = 0.0494$.

Quantitatively, the comparison between LSA predictions and VoF simulations is shown in figure 17 for the sinuous mode, and in figure 18 for the varicose mode, as functions of distance from the inlet. As we saw previously, in § 4.2, we consider only the near-field region, where the assumptions of linearity in LSA, mean profiles, and the exclusion of additional advection terms are reasonable. With decreasing gas shear layer thickness δ_G , the critical growth rate for both modes increases, leading to a faster manifestation of nonlinear effects. Consequently, the extent of the longitudinal domain shown in figures 17 and 18 is smaller with decreasing δ_G . For the critical varicose mode, shown in figure 18, the differences with VoF results are more noticeable. We speculate that this is due to a more significant departure from the assumed form of the mean velocity fields (2.8) as a function of x , which is more prevalent in the varicose case as depicted in figure 12. Nevertheless, there is good agreement overall between LSA and VoF in the near field.

5. Do dominant modes in the linear regime lead to breakup?

Based on the results from figure 6, it is expected that the large-scale sinuous modes, recorded for $\delta_G/H \gtrsim 0.3$, are responsible for sheet fragmentation, whereas the varicose modes, which have a much lower λ_{crit}/H , are presumed responsible for surface disturbances without appreciably affecting the liquid core due to their limited size. These ideas are tested by employing VoF simulations. We understand that the complexity of

Breakup of planar liquid sheets

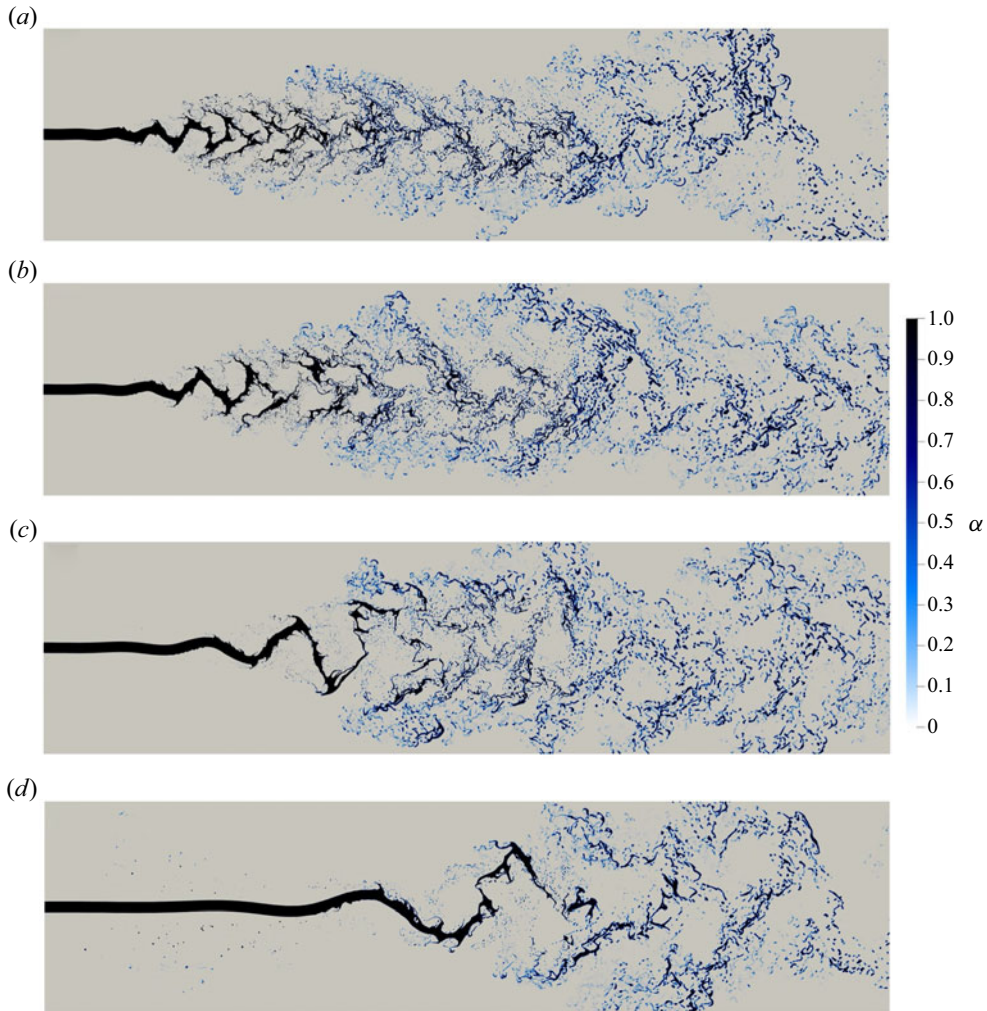


Figure 19. The VoF results under critical sinuous mode inlet conditions: (a) $\delta_G/H = 1/6$, (b) $\delta_G/H = 1/4$, (c) $\delta_G/H = 1/2$ and (d) $\delta_G/H = 1$.

three-dimensional (3-D) phenomena, as examined in other works (Jarrahbashi & Sirignano 2014; Zandian, Sirignano & Hussain 2017), is not fully captured in the present 2-D simulations; however, the main characteristics of the large-scale sinuous mode, which has been a central point in the present investigation, are captured relatively well in two dimensions. In fact, 3-D simulations, such as those shown previously in figure 1 or those presented in earlier work (Deshpande *et al.* 2015), do corroborate the presence of this large-scale mode in breaking up the sheet.

Both critical sinuous and varicose modes are imposed on the flow inlet as described in § 4. We consider eight cases corresponding to conditions given in table 1. Other cases – still within high-speed injection conditions – have been observed to have the same type of behaviour as reported here. The values employed for the gas shear layer thickness are $\delta_G = (H/6, H/4, H/2, H)$. The critical frequencies corresponding to these values of δ_G are, respectively, $\tilde{\omega}_{crit, sinuous} = (1.452, 1.0106, 0.6079, 0.3064)$ for the sinuous modes, and $\tilde{\omega}_{crit, varicose} = (10.25, 8.482, 5.19, 3.42)$ for the varicose modes.

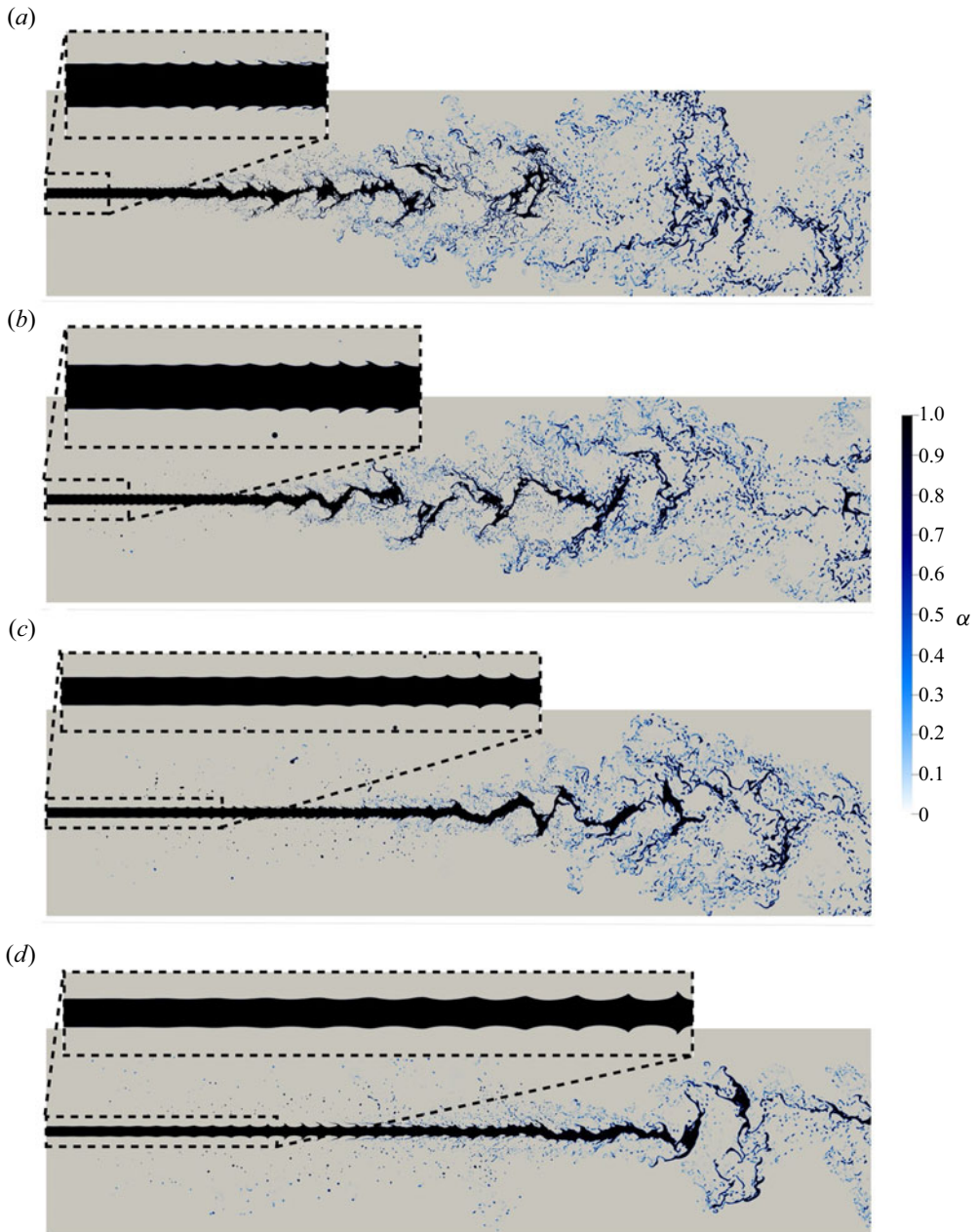


Figure 20. The VoF results under critical varicose mode inlet conditions: (a) $\delta_G/H = 1/6$, (b) $\delta_G/H = 1/4$, (c) $\delta_G/H = 1/2$ and (d) $\delta_G/H = 1$.

These critical frequencies are used in the imposed perturbations at the inlet. Since the effect of liquid shear layer thickness is negligible, a constant value $\delta_L = H/12$ is used.

The VoF results corresponding to the sinuous and varicose modes are shown respectively in figures 19 and 20. Since the varicose modes are small, close-up views of the near field are provided. From linear stability, $\lambda_{crit, sinuous}/H = (3.938, 5.326, 7.902, 14.513)$ correspond to cases with $\delta_G = (H/6, H/4, H/2, H)$; hence

the wavelength increases in proportion to the gas shear layer thickness. This behaviour is evident in the near field, and it is also observed in the breakup region, where visibly the length scale at breakup is consistently larger with increasing δ_G .

For the varicose mode, the development of the instabilities leads to the formation of cusps at the interface, which is progressively elongated due to the surrounding shear flow structure. Eventually, these cusps undergo breakup, but the liquid core remains intact. Further downstream, a sinuous type of structure develops. We speculate that the mode associated with this sinuous structure is activated by the nonlinear term in the Navier–Stokes equation. Since this occurs in a region where the gas shear layer thickness has grown considerably, once the sinuous mode becomes activated, it leads to an accelerated development and subsequent fragmentation of the sheet.

A frequency analysis is performed to quantify the results from figures 19 and 20. In this analysis, a Fourier decomposition of the vertical velocity, given by (4.8), is carried out as a function of x/H . The intensity of each Fourier mode is evaluated and normalized by the maximum magnitude of the modes, i.e. $|\hat{v}_n(x)|/(\max\{|\hat{v}_n(x)|, n = 1, \dots, N\})$, where N varies around 10^4 . The results are presented in terms of a spectrogram, shown in figures 21 and 22 for the sinuous and varicose modes. In these plots, the frequency pertaining to the Fourier decomposition is shown in the y -axis, and the streamwise coordinate in the x -axis. A dashed line is included to denote the imposed critical frequency, and a colour map is used to indicate the intensity of each Fourier mode. The spectrograms are plotted up to the respective breakup length for each case.

Examining figure 21 for the sinuous modes, the results show that the imposed inlet perturbation remains the most dominant mode throughout the entire domain, all the way to the breakup point. This implies that its dominance extends well beyond the linear regime, which is observed for all cases of δ_G/H . As we move away from the near field, other modes become activated as the process becomes nonlinear. For instance, for $\delta/H = 0.5$ (figure 21c), this nonlinear transition begins at $x/H \approx 10$; however, the critical imposed mode remains the strongest.

The story is quite different for the varicose modes shown in figure 22. A close-up view of the near-field region is included to aid in the visualization of the spectrogram. The results show that in the near field, the excited critical mode remains the largest one. This behaviour is also visually confirmed in figure 20. Further downstream, at $x/H \approx (7, 14, 25, 32)$ corresponding to $\delta_G = (H/6, H/4, H/2, H)$, lower-frequency modes become excited and subsequently dominate the process, i.e. the critical varicose mode becomes inconsequential in the nonlinear regime and plays an insignificant role in the breakup process.

6. Perturbation energy analysis

The objective of the perturbation energy analysis is to identify the most influential factors affecting growth in both sinuous and varicose modes. This analysis bears similarities with the work of Boomkamp & Miesen (1996), where a temporal instability in a two-phase shear layer was considered. However, in our current work, we are studying a spatially growing disturbance, which leads to some important terms not cancelling out and contributing significantly to the growth of the sinuous mode.

We begin by rewriting the perturbation equations (2.7b) and (2.7c) in vector form, and taking the inner product with the perturbation velocity, yielding

$$\left[\rho \frac{\partial \mathbf{u}'}{\partial t} + \rho \bar{u} \frac{\partial \mathbf{u}'}{\partial x} + \rho v' \frac{d\bar{u}}{dy} \mathbf{e}_x \right] \cdot \mathbf{u}' = (\nabla \cdot \mathbf{T}') \cdot \mathbf{u}', \quad (6.1)$$

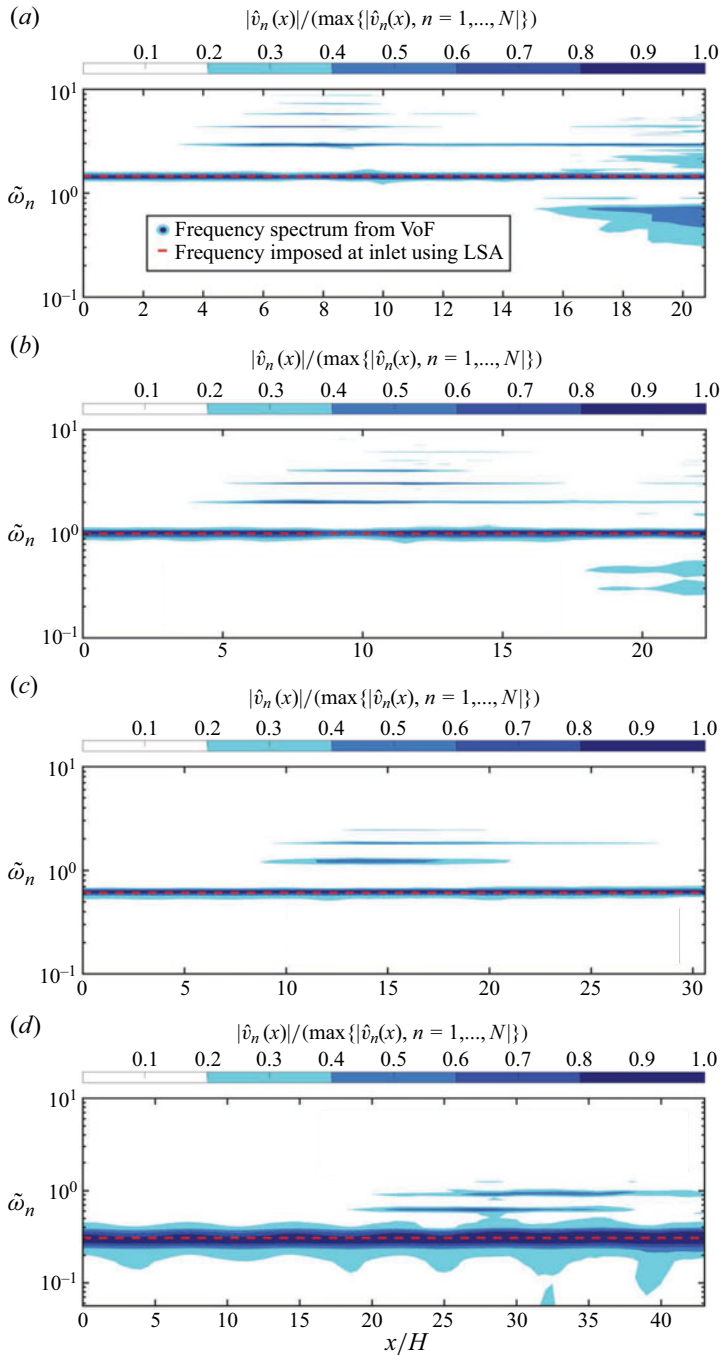


Figure 21. Frequency plots for critical sinuous modes: (a) $\delta_G/H = 1/6$, (b) $\delta_G/H = 1/4$, (c) $\delta_G/H = 1/2$ and (d) $\delta_G/H = 1$.

where T' is the stress tensor, namely $T_{ij} = -p'\delta_{ij} + \mu(\partial u'_i/\partial x_j + \partial u'_j/\partial x_i)$. Considering a liquid region $\Omega_L = [0, H/2] \times [0, \lambda]$ and a gas region $\Omega_G = [H/2, W] \times [0, \lambda]$ as shown in figure 23, the above expression is integrated over $\Omega = \Omega_L \cup \Omega_G$. Here, λ is the wavelength, i.e. $2\pi/k_R$, corresponding to the normal mode representation of a given

Breakup of planar liquid sheets

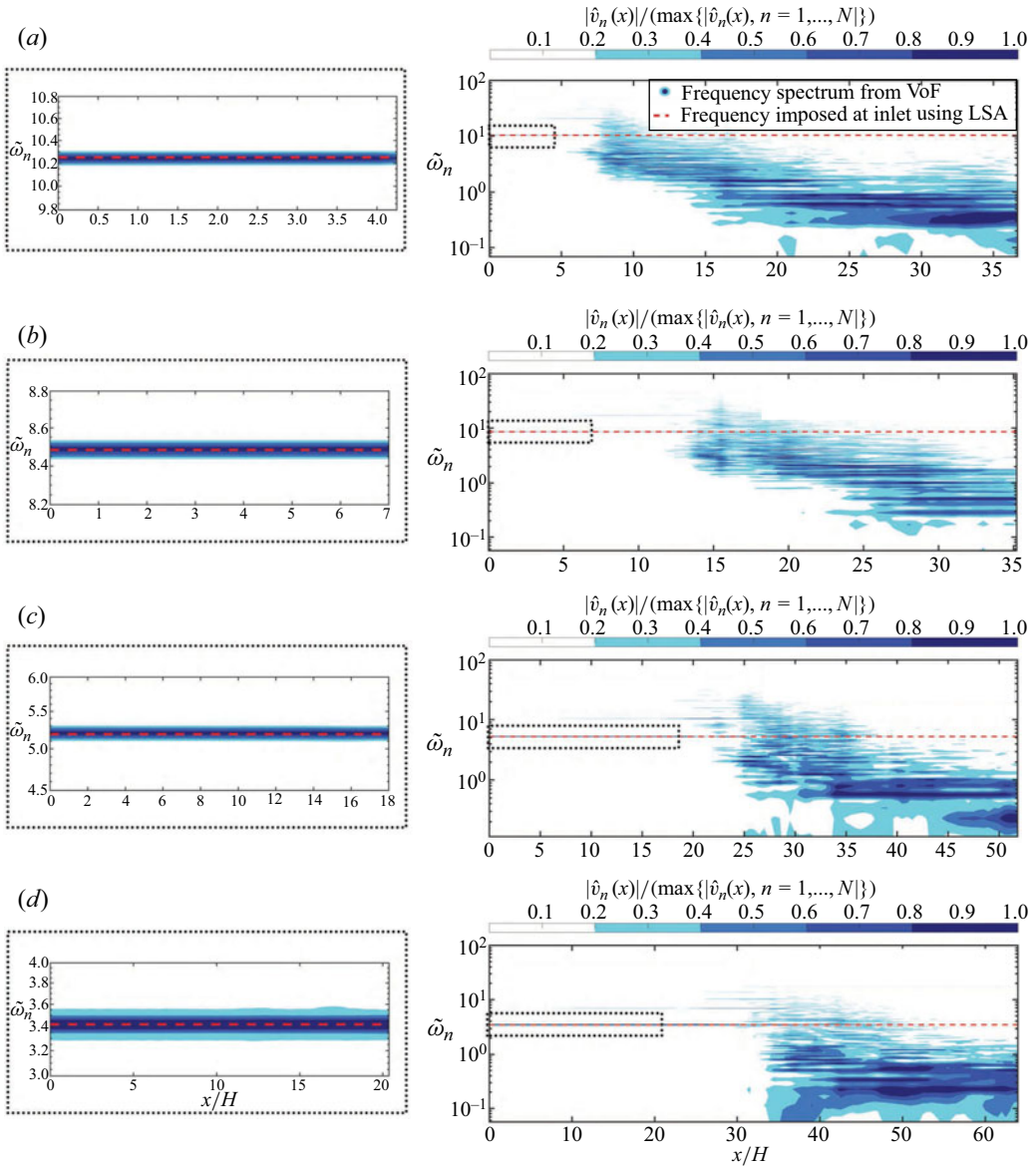


Figure 22. Frequency plots for critical varicose modes: (a) $\delta_G/H = 1/6$, (b) $\delta_G/H = 1/4$, (c) $\delta_G/H = 1/2$ and (d) $\delta_G/H = 1$.

perturbation. The integration results in

$$\begin{aligned}
 & \int_{\Omega} \rho \frac{\partial \mathbf{u}'}{\partial t} \cdot \mathbf{u}' \, dS + \int_{\Omega} \rho \bar{u} \frac{\partial \mathbf{u}'}{\partial x} \cdot \mathbf{u}' \, dS + \int_{\Omega} \left(\rho v' \frac{d\bar{u}}{dy} e_x \right) \cdot \mathbf{u}' \, dS \\
 & = \int_{\Omega} \nabla \cdot (\mathbf{T}' \cdot \mathbf{u}') \, dS - \int_{\Omega} \mathbf{T}' : \nabla \mathbf{u}' \, dS,
 \end{aligned} \tag{6.2}$$

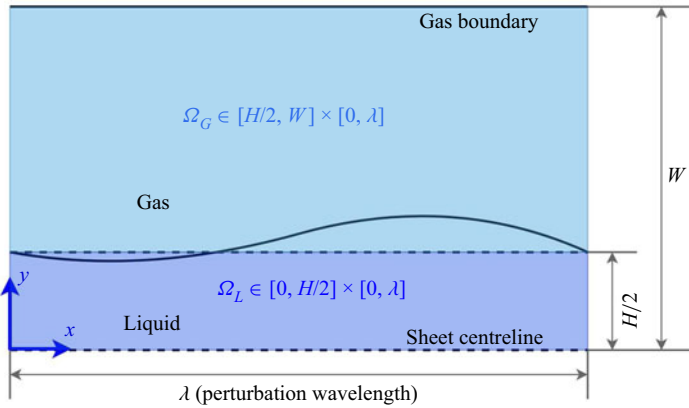


Figure 23. Schematic representation of the domain considered for the perturbation energy analysis.

where the right-hand side has been re-expressed with the introduction of the viscous dissipation term. This equation can be manipulated further by first noting that

$$\mathbf{T}' \cdot \mathbf{u}' = \begin{bmatrix} T'_{xx}u' + T'_{xy}v' \\ T'_{xy}u' + T'_{yy}v' \end{bmatrix} \quad (6.3)$$

and

$$\mathbf{T}' : \nabla \mathbf{u}' = 2\mu E_{ij}E_{ij} = \phi = 2\mu \left[\left(\frac{\partial u'}{\partial x} \right)^2 + \frac{1}{2} \left(\frac{\partial u'}{\partial y} + \frac{\partial v'}{\partial x} \right)^2 + \left(\frac{\partial v'}{\partial y} \right)^2 \right]. \quad (6.4)$$

Introducing these expressions into (6.2) yields, after some work,

$$\begin{aligned} & \underbrace{\frac{1}{2} \int_{\Omega} \frac{\partial(\rho(u'^2 + v'^2))}{\partial t} dS + \frac{1}{2} \int_{\Omega} \bar{u} \frac{\partial(\rho(u'^2 + v'^2))}{\partial x} dS}_{KE} \\ &= \underbrace{- \int_{\Omega} \rho u' v' \frac{d\bar{u}}{dy} dS}_{PROD} \\ &+ \underbrace{\int_0^{\lambda} (T'_{xy}u' + T'_{yy}v'|_{y=H/2,L}) dx - \int_0^{\lambda} (T'_{xy}u' + T'_{yy}v'|_{y=H/2,G}) dx}_{INT} \\ &+ \underbrace{\int_0^{H/2} (T'_{xx}u' + T'_{xy}v'|_{x=0}^{x=\lambda}) dy}_{STR_{x,L}} + \underbrace{\int_{H/2}^W (T'_{xx}u' + T'_{xy}v'|_{x=0}^{x=\lambda}) dy}_{STR_{x,G}} + \underbrace{\int_{\Omega} -\phi dS}_{DIS}, \quad (6.5) \end{aligned}$$

where the quantities evaluated at $(y = H/2, L)$ and $(y = H/2, G)$ correspond to the liquid and gas sides of the interface, respectively. In the spectral discretization for velocity and pressure, both liquid and gas phases contain an interfacial node precisely to evaluate the corresponding interfacial quantities. Each bracketed term above can be separated into its liquid or gas phase, with the exception of $STR_{x,G}$ and $STR_{x,L}$, which are already separated in this fashion.

Breakup of planar liquid sheets

The term KE in (6.5) represents the time rate of change of kinetic energy of the perturbation following the mean flow field, $\bar{u}(y)$. The contributions to KE are given by terms denoted as $PROD$, INT , STR_x and DIS . The term $PROD$ represents the energy production due to the Reynolds shear stress ($u'v'$). A similar quantity ($-\langle u'v' \rangle d\langle \bar{u} \rangle / dy$) is mentioned in Pope (2000), where it appears as an energy sink in the mean flow field kinetic energy and a source term for the turbulent kinetic energy. In the present work, this connection is not entirely analogous since we employ a mean flow field that is treated using error function profiles (see (2.8)). Nevertheless, $PROD$ represents a source in the evolution of KE .

The next term, INT , represents the work done on the interface, which can be divided into normal and shear contributions as

$$\begin{aligned}
 INT &= \underbrace{\int_0^\lambda [[T'_{yy}v'|_{y=H/2,L} - [T'_{yy}v'|_{y=H/2,G}]dx}_{normal} \\
 &+ \underbrace{\int_0^\lambda [[T'_{xy}u'|_{y=H/2,L} - [T'_{xy}u'|_{y=H/2,G}]dx}_{shear} \\
 &= \underbrace{\int_0^\lambda \gamma \frac{\partial^2 \eta}{\partial x^2} \Big|_{H/2} \times v'_{y=H/2,L} dx}_{normal} \\
 &+ \underbrace{\int_0^\lambda T'_{xy}|_{y=H/2,L} \times (u'_{y=H/2,L} - u'_{y=H/2,G}) dx}_{shear} \\
 &= \underbrace{\int_0^\lambda \gamma \frac{\partial^2 \eta}{\partial x^2} \Big|_{H/2} \times v'_{y=H/2,L} dx}_{normal} \\
 &+ \underbrace{\int_0^\lambda \mu_L \left(\frac{\partial u'}{\partial y} + \frac{\partial v'}{\partial x} \right)_{y=H/2,L} \times \eta \left(\frac{\partial \bar{u}_G}{\partial y} - \frac{\partial \bar{u}_L}{\partial y} \right)_{y=H/2} dx}_{shear} \\
 &= \underbrace{\int_0^\lambda \gamma \frac{\partial^2 \eta}{\partial x^2} \Big|_{H/2} \times v'_{y=H/2,L} dx}_{normal} \\
 &+ \underbrace{\int_0^\lambda \mu_L \left(\frac{\partial u'}{\partial y} + \frac{\partial v'}{\partial x} \right)_{y=H/2,L} \times \eta \left(\frac{\partial \bar{u}_L}{\partial y} \Big|_{y=H/2} \left(\frac{\mu_L}{\mu_G} - 1 \right) dx}_{shear}. \tag{6.6}
 \end{aligned}$$

The normal term is obtained by applying the normal jump condition (2.12a) and noting that v' is continuous at the interface (2.12d). This results in the introduction of the surface tension force. The shear term is manipulated by introducing the shear jump condition (2.12b) and recognizing that $d^2\bar{u}_L/dy^2 = d^2\bar{u}_G/dy^2 = 0$ as a result of the mean profiles

δ_G/H	KE_L	KE_G	$PROD_L$	$PROD_G$	INT	$STR_{x,L}$	$STR_{x,G}$	DIS_L	DIS_G
1/6	0.427	0.573	0.022	0.726	0.089	0.036	0.195	-0.004	-0.055
1/4	0.409	0.591	0.014	0.733	0.050	0.025	0.217	-0.002	-0.031
1/2	0.425	0.575	0.007	0.747	0.026	0.015	0.224	-0.001	-0.015
1	0.387	0.613	0.003	0.781	0.010	0.006	0.207	-0.001	-0.005

Table 3. Energy budget for critical sinuous modes ($Re_L = 12955$ and $Oh_L = 0.0134$).

considered here (see (2.8)). This gives $T'_{xy}|_{y=H/2,L} = T'_{xy}|_{y=H/2,G}$. By the continuity of horizontal velocity (2.12c), the perturbation velocities ($u'_{y=H/2,L} - u'_{y=H/2,G}$) can be substituted by mean velocity derivatives. Furthermore, by the continuity of shear in the mean flow state (2.9), the ratio of viscosities is introduced, which shows that as $\mu_L \rightarrow \mu_G$, the entire shear term in INT disappears.

The next term in (6.5) represents the work done by the stresses on the lateral or vertical faces of Ω and is given by STR_x . This term can be divided further into the working of pressure, viscous normal and viscous shear forces, namely

$$STR_x = \underbrace{\int_{y=0}^W [-p'u']_{x=0}^\lambda dy}_{\text{pressure}} + \underbrace{\int_{y=0}^W \left[2\mu \frac{\partial u'}{\partial x} u' \right]_{x=0}^\lambda dy}_{\text{viscous normal}} + \underbrace{\int_{y=0}^W \left[\mu \left(\frac{\partial u'}{\partial y} + \frac{\partial v'}{\partial x} \right) v' \right]_{x=0}^\lambda dy}_{\text{viscous shear}}. \quad (6.7)$$

Interestingly, the STR_x terms are exactly zero for a temporally growing stability (Boomkamp & Miesen 1996) since these terms are periodic at the lateral faces of Ω . In the present work, due to the spatially growing disturbance, this periodicity does not occur, and STR_x remains finite. Finally, the viscous dissipation of the perturbed flow is denoted by DIS , and this quantity is always negative and hence opposes the growth of KE .

To identify the responsible physics associated with the growth of instability modes as a function of gas shear layer thickness, we compute each term in the energy budget balance equation (6.5). This is done for both critical sinuous and varicose modes using the previous nominal conditions of table 1. Finally, all quantities are normalized by $KE = KE_L + KE_G$. First, we consider the energy budget for critical sinuous modes, which is presented in table 3. The results show that the rate of perturbation kinetic energy in liquid (KE_L) is slightly lower than its gas counterpart (KE_G), despite the fact that the density ratio is $\rho_G/\rho_L = 0.075$. This behaviour is explained by examining the modulus of horizontal and vertical eigenfunctions, i.e. $|\hat{u}(y)|$ and $|\hat{v}(y)|$. These quantities are plotted as functions of δ_G/H in figure 24. From these plots, it is evident that the extent of Ω_G is substantially larger than that of Ω_L , and that both $|\hat{u}(y)|$ and $|\hat{v}(y)|$ remain relatively high over a much bigger region on the gas side. Also, with larger values of δ_G , this behaviour becomes more pronounced, particularly for $|\hat{v}(y)|$. These effects combine to offset the density disparity between liquid and gas, yielding values for KE_G and KE_L that are similar in magnitude.

Out of the terms contributing to the kinetic energy growth of the sinuous perturbation, the Reynolds shear term $PROD$, in particular $PROD_G$, has the greatest influence. However, in the liquid phase, $PROD_L$ is essentially negligible, hovering at approximately 2% of the total kinetic energy growth, and declines with increasing δ_G/H . This is due to relatively low values of $(u'v')$ combined with a fast decay of $d\bar{u}/dy$ on the liquid side.

The work done at the interface, INT , has a low value and decreases with increasing δ_G . It can be shown that the normal contributions are negative and thus are interpreted as being restorative, i.e. driving towards the decay of the perturbation. On the other hand, the

Breakup of planar liquid sheets

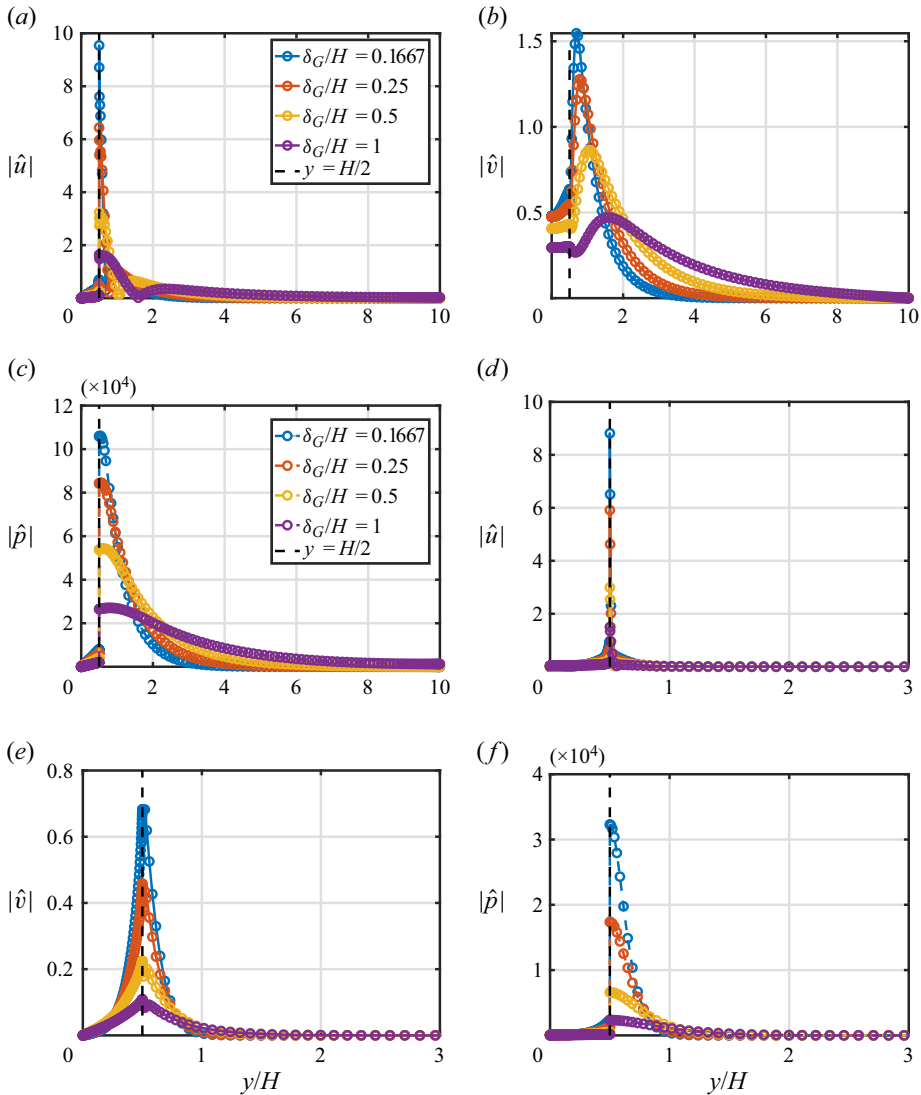


Figure 24. Plots of absolute values of velocity and pressure perturbations for different δ_G/H values. For all the plots, the interfacial displacement is 1.5% of the liquid sheet thickness: (a) $|\hat{u}|$, critical sinuous mode; (b) $|\hat{v}|$, critical sinuous mode; (c) $|\hat{p}|$, critical sinuous mode; (d) $|\hat{u}|$, critical varicose mode; (e) $|\hat{v}|$, critical varicose mode; (f) $|\hat{p}|$, critical varicose mode.

tangential contributions are significantly greater and are positive, leading to the growth of the instability. Nevertheless, the relative magnitude of this *INT* term is secondary to the more dominant contributors from *PROD* and *STR_x*.

With regard to the work done by the lateral stresses, their effect is appreciable but only for the gas phase, i.e. $STR_{x,G} \gg STR_{x,L}$. Each of the components of $STR_{x,G}$ is inspected further and shown in table 4, where the pressure contribution is by far the most dominant factor. The workings of shear and normal stresses on the lateral faces of Ω are orders of magnitude smaller. Finally, the viscous dissipation *DIS* plays a minor role in the sinuous mode development, and it is lower in the liquid compared to the gas. This is due to the

δ_G/H	$STR_{x,G}$	Pressure	Viscous normal	Viscous shear
1/6	0.1951	0.1951	5.67×10^{-4}	-5.034×10^{-5}
1/4	0.2171	0.2171	4.95×10^{-5}	-2.5868×10^{-5}
1/2	0.2239	0.2239	3.45×10^{-5}	-1.1228×10^{-5}
1	0.2068	0.2068	2.525×10^{-5}	-5.127×10^{-6}

Table 4. Components of STR_x (lateral working of stresses) for the critical sinuous modes ($Re_L = 12\,955$ and $Oh_L = 0.0134$).

δ_G/H	KE_L	KE_G	$PROD_L$	$PROD_G$	INT	$STR_{x,L}$	$STR_{x,G}$	DIS_L	DIS_G
1/6	0.641	0.359	0.006	0.681	1.270	0.031	-0.017	-0.1159	-0.850
1/4	0.644	0.356	0.010	0.678	1.311	0.025	-0.016	-0.120	-0.878
1/2	0.659	0.341	0.016	0.664	1.204	0.020	-0.015	-0.098	-0.785
1	0.670	0.330	0.015	0.656	1.160	0.017	-0.012	-0.086	-0.744

Table 5. Energy budget for critical varicose modes ($Re_L = 12\,955$ and $Oh_L = 0.0134$).

δ_G/H	$STR_{x,G}$	Pressure	Viscous normal	Viscous shear
1/6	-0.017	-0.0165	2.21×10^{-5}	-4.8874×10^{-4}
1/4	-0.0162	-0.01583	1.394×10^{-5}	-3.8162×10^{-4}
1/2	-0.0157	-0.01548	5.988×10^{-6}	-2.2473×10^{-4}
1	-0.0128	-0.01265	2.835×10^{-6}	-1.4789×10^{-4}

Table 6. Components of STR_x (lateral working of stresses) for the critical varicose modes ($Re_L = 12\,955$ and $Oh_L = 0.0134$).

velocity gradients being more pronounced in the gas region, and this region being much larger.

The calculations are repeated for the critical varicose modes, and the results are presented in table 5. Unlike the critical sinuous modes, KE_L for critical varicose modes is noticeably higher compared to KE_G . This can be explained by considering that the magnitudes $|\hat{u}(y)|$ and $|\hat{v}(y)|$ in the varicose case decay more rapidly than in the sinuous case as we move away from the interface.

The working of Reynolds shear, $PROD$, is the second highest contributor to the growth of the varicose mode, with the gas side having the most significant influence. In terms of its relative magnitude, it is quite similar to the critical sinuous mode. The interfacial term INT is the most significant contributor, and its value is significantly higher when compared to the sinuous mode. The tangential component of INT is responsible for this behaviour. The normal component governed by surface tension is again negative and thus restorative.

The working of the lateral stresses, STR_x , is relatively small for the varicose mode and negative on the gas side. The components of this term on the gas side are included in table 6. Similarly to the sinuous mode, the pressure contribution is orders of magnitude greater than the viscous normal or tangential components. Nevertheless, relative to the kinetic energy term, STR_x is much smaller for the varicose mode, which highlights a notable difference in the development of this type of instability. Another significant difference is the dissipation term, which is substantially higher for the varicose mode. This dissipation is confined to a small region around the interface, with larger values on

the gas side. For the varicose mode, the peak values for DIS are multiple times higher than for the sinuous mode, explaining the discrepancy observed.

7. Summary and conclusions

The present work has analysed the growth of large-scale sinuous modes under high-speed injection conditions utilizing a combination of two-dimensional (2-D) volume-of-fluid (VoF) and spatial linear stability analysis (LSA). In a manner similar to the coflowing case, the shear layer thickness δ_G also plays a highly influential role in the present liquid injection into a quiescent medium. For small values of δ_G/H , the growth curve $-k_I$ versus wavenumber k_R displays a single prominent peak, which matches between varicose and sinuous modes. However, as δ_G/H grows beyond $O(10^{-1})$, a second peak develops for the sinuous mode, at a much larger wavelength greater than H . At some threshold value of δ_G/H , which is approximately 0.3, this larger-scale mode becomes the critical one and becomes progressively more dominant with increasing values of δ_G/H . For the varicose mode, the shape of the growth curve does not change much as δ_G/H increases. Interestingly, the shear layer thickness in the liquid plays a very secondary role in the development of these instabilities. For liquid injections occurring at lower velocities, LSA predictions do not show the appearance of this dominant large-scale sinuous mode. At these lower speeds, the growth rate curve retains a single peak. This demonstrates that the manifestation of this large-scale mode is a distinguishing characteristic of high-speed injection.

Additional LSA calculations were run at various values of Oh and Re within the atomization regime. The results show that for $\delta_G/H \geq 0.3$, the wavelength of the critical sinuous mode for all cases considered collapses onto a single curve, namely $\lambda_{crit,sinuous}/H = 14.26 (\delta_G/H)^{0.766}$. For values $\delta/H \lesssim O(10^{-1})$, the predictions for $\lambda_{crit,sinuous}/H$ still scale with $(\delta_G/H)^p$; however, each curve is distinct, depending on its respective values of Oh_L and Re_L . Also, for $\delta/H < O(10^{-1})$, the difference between the sinuous and varicose mode growth rate curves is essentially the same, with minor differences occurring in the lower wavenumber range.

Two-dimensional VoF simulations are employed to evaluate the LSA assumptions – explicitly, the neglect of additional advection terms in the governing equations, and the assumed form of mean velocity profiles. It is demonstrated that the LSA assumptions hold within the near field, which ranges along the streamwise direction from approximately $6H$ to $15H$ for the large-scale sinuous mode, and from approximately $2H$ to $15H$ for the small-scale varicose mode. The range in the extent of this domain is linked intrinsically with the type of instability considered.

Carrying out the calculation of instabilities beyond the linear regime with the use of 2-D VoF simulations, the results show that when the critical sinuous mode predicted from LSA is imposed at the inlet, it continues to dominate well into the nonlinear regime. Moreover, based on frequency analysis, these large-scale sinuous modes are responsible for the breakup of the sheet. Simulation results where the critical varicose mode is imposed show that it grows quickly and can disrupt the surface of the sheet, breaking it up. However, since its associated wavelength is substantially smaller than H , it does not disturb the liquid core. At some point downstream of injection, a large-scale sinuous mode develops, which is ultimately responsible for the sheet breakup.

With regard to 3-D behaviour akin to the simulations depicted in [figure 1](#), it can be inferred from the previous analysis that for relatively small shear layer thickness, either

the varicose or small-scale sinuous mode will be critical. This implies that these modes will develop and lead to the breakup of the surface of the sheet, producing a population of small droplets, and this behaviour is consistent with 3-D simulations shown in figure 1. Further downstream, as δ_G grows, and the large-scale sinuous mode is activated by the nonlinearity of the underlying dynamics, this mode becomes dominant, and its growth will lead directly to the fragmentation of the sheet.

An energy analysis is considered, where an examination of the contributing elements to the growth of perturbation kinetic energy is performed. These elements are found to be the working of the Reynolds shear stress, interfacial forces, lateral stress and viscous dissipation. For the sinuous mode, the most influential contributing factor is the working of the Reynolds shear stress (*PROD*), particularly on the gas side. This is followed in order of significance by the working of lateral stress (*STR_x*), also on the gas side. This lateral stress is further subdivided into pressure, viscous normal and viscous shear. Among these components, the working of the pressure is orders of magnitude larger than the others. In contrast, for the varicose mode, it is the shear stress at the interface (*INT*) that plays a dominant role, followed by the Reynolds shear term. The surface tension force remains a small negative contributor for both sinuous and varicose critical modes, indicating its tendency to suppress the instability. But in both cases, surface tension has a negligible effect. Finally, the viscous dissipation is relatively important for the varicose mode but almost insignificant for the larger sinuous mode, indicating that for the large sinuous mode, there is little resistance to the development of this instability.

Funding. Support from the National Science Foundation (no. 1703825) is gratefully acknowledged with R. Joslin, its programme director.

Declaration of interests. The authors report no conflict of interest.

Author ORCID.

① Mohan Ananth <https://orcid.org/0000-0002-8420-2421>;

② Mario F. Trujillo <https://orcid.org/0000-0002-9546-8794>.

Appendix. Description of LSA

The normal mode decomposition is first substituted into the governing equations (2.7), giving

$$k [i\hat{u}_q] + \left[\frac{d\hat{v}_q}{dy} \right] = 0, \tag{A1a}$$

$$k^2 [v_q \hat{u}_q] + k \left[i\bar{u}_q \hat{u}_q + i \frac{1}{\rho_q} \hat{p}_q \right] + \left[-i\omega \hat{u}_q + \hat{v}_q \frac{d\bar{u}_q}{dy} - v_q \frac{d^2 \hat{u}_q}{dy^2} \right] = 0 \tag{A1b}$$

and

$$k^2 [v_q \hat{v}_q] + k [i\bar{u}_q \hat{v}_q] + \left[-i\omega \hat{v}_q + \frac{1}{\rho_q} \frac{d\hat{p}_q}{dy} - v_q \frac{d^2 \hat{v}_q}{dy^2} \right] = 0, \tag{A1c}$$

where in this form we are explicitly denoting liquid ($q = L$) or gas ($q = G$) phase variables and properties. This normal mode decomposition is also substituted into the boundary

Breakup of planar liquid sheets

conditions (2.11) and interfacial constraints (2.12), respectively, yielding

$$\text{varicose} \quad \left[\frac{d\hat{u}_L}{dy} \right]_{y=0} = 0, \quad \left[\hat{v}_L \right]_{y=0} = 0, \quad \left[\frac{d\hat{p}_L}{dy} \right]_{y=0} = 0, \quad (\text{A2a})$$

$$\text{sinuous} \quad \left[\hat{u}_L \right]_{y=0} = 0, \quad \left[\frac{d\hat{v}_L}{dy} \right]_{y=0} = 0, \quad \left[\hat{p}_L \right]_{y=0} = 0, \quad (\text{A2b})$$

$$\text{varicose and sinuous} \quad \left[\frac{d\hat{u}_G}{dy} \right]_{y=W} = 0, \quad \left[\hat{v}_G \right]_{y=W} = 0, \quad \left[\frac{d\hat{p}_G}{dy} \right]_{y=W} = 0, \quad (\text{A2c})$$

and

$$k^2 \left(\gamma [\hat{u}_L - \hat{u}_G] \left[\frac{d\bar{u}_L}{dy} - \frac{d\bar{u}_G}{dy} \right]^{-1} \right) \Big|_{y=H/2} + \left(\left[\hat{p}_L - 2\mu_L \frac{d\hat{v}_L}{dy} \right] - \left[\hat{p}_G - 2\mu_G \frac{d\hat{v}_G}{dy} \right] \right) \Big|_{y=H/2} = 0, \quad (\text{A3a})$$

$$k^2 \left(\mu_L \bar{u}_L \hat{v}_L - \mu_G \bar{u}_G \hat{v}_G \right) \Big|_{y=H/2} + k \left(\mu_L \left[-i\bar{u}_L \frac{d\hat{u}_L}{dy} - \omega \hat{v}_L \right] - \mu_G \left[-i\bar{u}_G \frac{d\hat{u}_G}{dy} - \omega \hat{v}_G \right] \right) \Big|_{y=H/2} + \left(\mu_L \left[i\omega \frac{d\hat{u}_L}{dy} - \hat{v}_L \frac{d^2 \bar{u}_L}{dy^2} \right] - \mu_G \left[i\omega \frac{d\hat{u}_G}{dy} - \hat{v}_G \frac{d^2 \bar{u}_G}{dy^2} \right] \right) \Big|_{y=H/2} = 0, \quad (\text{A3b})$$

$$k([\bar{i}\bar{u}_L \hat{u}_L] - [\bar{i}\bar{u}_G \hat{u}_G]) \Big|_{y=H/2} + \left(\left[\hat{v}_L \frac{d\bar{u}_L}{dy} - i\omega \hat{u}_L \right] - \left[\hat{v}_G \frac{d\bar{u}_G}{dy} - i\omega \hat{u}_G \right] \right) \Big|_{y=H/2} = 0 \quad (\text{A3c})$$

and

$$(\hat{v}_L - \hat{v}_G) \Big|_{y=H/2} = 0. \quad (\text{A3d})$$

Here, the substitution of the normal mode treatment has already been done for the kinematic condition back in (2.14).

In the solution of (A1), (A2) and (A3), the Chebyshev spectral method (Boyd 2001) is employed. The liquid and gas domains are divided into N_L and N_G numbers of Gauss–Lobatto (G–L) points, respectively. These points are projections of equidistant points on a unit semicircle on the x -axis. Hence G–L points agglomerate near the interface and the boundaries. In order to accommodate this domain division using G–L points, the non-dimensional vertical coordinate is transformed to vary in $[-1, 1]$ in both the liquid and gas domains by using the transformation

$$\text{liquid} \quad \tilde{y}_L = 4 \frac{y}{H} - 1, \quad \text{for } \frac{y}{H} \in [0, 1/2], \quad (\text{A4})$$

$$\text{gas} \quad \tilde{y}_G = \frac{2(y/H - 1/2)}{W/H - 1/2} - 1, \quad \forall \frac{y}{H} \in [1/2, W/H], \quad (\text{A5})$$

where W/H is the ratio of the height of the domain from the liquid centreline (W) to the liquid sheet thickness (H).

After non-dimensionalization and coordinate transformation (A4), the governing equations (A1) in the liquid phase become

$$\tilde{k} [i\tilde{u}_L] + \left[4 \frac{d\tilde{v}_L}{d\tilde{y}_L} \right] = 0, \tag{A6a}$$

$$\tilde{k}^2 \left[\frac{1}{Re_L} \tilde{u}_L \right] + \tilde{k} [i\tilde{u}_L\tilde{u}_L + i\tilde{p}_L] + \left[-i\tilde{\omega}\tilde{u}_L + 4\tilde{v}_L \frac{d\tilde{u}_L}{d\tilde{y}_L} - 16 \frac{1}{Re_L} \frac{d^2\tilde{u}_L}{d\tilde{y}_L^2} \right] = 0 \tag{A6b}$$

and

$$\tilde{k}^2 \left[\frac{1}{Re_L} \tilde{v}_L \right] + \tilde{k} [i\tilde{u}_L\tilde{v}_L] + \left[-i\tilde{\omega}\tilde{v}_L + 4 \frac{d\tilde{p}_L}{d\tilde{y}_L} - 16 \frac{1}{Re_L} \frac{d^2\tilde{v}_L}{d\tilde{y}_L^2} \right] = 0. \tag{A6c}$$

Similarly, the governing equation for gas yields

$$\tilde{k} [i\tilde{u}_G] + \left[\frac{4}{2W/H - 1} \frac{d\tilde{v}_G}{d\tilde{y}_G} \right] = 0, \tag{A7a}$$

$$\begin{aligned} \tilde{k}^2 \left[\left(\frac{\rho_L}{\rho_G} \frac{\mu_G}{\mu_L} \right) \frac{1}{Re_L} \tilde{u}_G \right] + \tilde{k} \left[i\tilde{u}_G\tilde{u}_G + i \left(\frac{\rho_L}{\rho_G} \right) \tilde{p}_G \right] \\ + \left[-i\tilde{\omega}\tilde{u}_G + \frac{4}{2W/H - 1} \tilde{v}_G \frac{d\tilde{u}_G}{d\tilde{y}_G} - \frac{16}{(2W/H - 1)^2} \left(\frac{\rho_L}{\rho_G} \frac{\mu_G}{\mu_L} \right) \frac{1}{Re_L} \frac{d^2\tilde{u}_G}{d\tilde{y}_G^2} \right] = 0 \end{aligned} \tag{A7b}$$

and

$$\begin{aligned} \tilde{k}^2 \left[\left(\frac{\rho_L}{\rho_G} \frac{\mu_G}{\mu_L} \right) \frac{1}{Re_L} \tilde{v}_G \right] + \tilde{k} [i\tilde{u}_G\tilde{v}_G] \\ + \left[-i\tilde{\omega}\tilde{v}_G + \frac{4}{2W/H - 1} \left(\frac{\rho_L}{\rho_G} \right) \frac{d\tilde{p}_G}{d\tilde{y}_G} - \frac{16}{(2W/H - 1)^2} \left(\frac{\rho_L}{\rho_G} \frac{\mu_G}{\mu_L} \right) \frac{1}{Re_L} \frac{d^2\tilde{v}_G}{d\tilde{y}_G^2} \right] = 0. \end{aligned} \tag{A7c}$$

The boundary conditions at the liquid centreline and the gas boundary after non-dimensionalization and coordinate transformation yield

$$\text{varicose} \quad \left[\frac{d\tilde{u}_L}{d\tilde{y}_L} \right]_{\tilde{y}_L=-1} = 0, \quad \left[\tilde{v}_L \right]_{\tilde{y}_L=-1} = 0, \quad \left[\frac{d\tilde{p}_L}{d\tilde{y}_L} \right]_{\tilde{y}_L=-1} = 0, \tag{A8a}$$

$$\text{sinuous} \quad \left[\tilde{u}_L \right]_{\tilde{y}_L=-1} = 0, \quad \left[\frac{d\tilde{v}_L}{d\tilde{y}_L} \right]_{\tilde{y}_L=-1} = 0, \quad \left[\tilde{p}_L \right]_{\tilde{y}_L=-1} = 0, \tag{A8b}$$

$$\text{varicose and sinuous} \quad \left[\frac{d\tilde{u}_G}{d\tilde{y}_G} \right]_{\tilde{y}_G=+1} = 0, \quad \left[\tilde{v}_G \right]_{\tilde{y}_G=+1} = 0, \quad \left[\frac{d\tilde{p}_G}{d\tilde{y}_G} \right]_{\tilde{y}_G=+1} = 0. \tag{A8c}$$

Breakup of planar liquid sheets

Finally, the non-dimensional interfacial constraints after the coordinate transformation are given by the equations

$$\tilde{k}^2 \left[\frac{1}{2We_L} [(\tilde{u}_L|_{\tilde{y}_L=+1} - \tilde{u}_G|_{\tilde{y}_G=-1}) \left[4 \left(\frac{d\tilde{u}_L}{d\tilde{y}_L} \Big|_{\tilde{y}_L=+1} - \frac{4}{2W/H-1} \left(\frac{d\tilde{u}_G}{d\tilde{y}_G} \Big|_{\tilde{y}_G=-1} \right) \right]^{-1} \right] \right. \\ \left. + \left[\left(\tilde{p}_L - \frac{8}{Re_L} \frac{d\tilde{v}_L}{d\tilde{y}_L} \Big|_{\tilde{y}_L=+1} - \left(\tilde{p}_G - \frac{8}{2W/H-1} \frac{\mu_G}{\mu_L} \frac{1}{Re_L} \frac{d\tilde{v}_G}{d\tilde{y}_G} \Big|_{\tilde{y}_G=-1} \right) \right] = 0, \quad (A9a)$$

$$\tilde{k}^2 \left[(\tilde{u}_L \tilde{v}_L|_{\tilde{y}_L=+1} - \frac{\mu_G}{\mu_L} (\tilde{u}_G \tilde{v}_G|_{\tilde{y}_G=-1}) \right] \\ + \tilde{k} \left[\left(-i4\tilde{u}_L \frac{d\tilde{u}_L}{d\tilde{y}_L} - \tilde{\omega} \tilde{v}_L \Big|_{\tilde{y}_L=+1} - \frac{\mu_G}{\mu_L} \left(-i \frac{4}{2W/H-1} \tilde{u}_G \frac{d\tilde{u}_G}{d\tilde{y}_G} - \tilde{\omega} \tilde{v}_G \Big|_{\tilde{y}_G=-1} \right) \right] \\ + \left[\left(i4\tilde{\omega} \frac{d\tilde{u}_L}{d\tilde{y}_L} - 16\tilde{v}_L \frac{d^2\tilde{u}_L}{d\tilde{y}_L^2} \Big|_{\tilde{y}_L=+1} \right. \right. \\ \left. \left. - \frac{\mu_G}{\mu_L} \left(i \frac{4}{2W/H-1} \tilde{\omega} \frac{d\tilde{u}_G}{d\tilde{y}_G} - \frac{16}{(2W/H-1)^2} \tilde{v}_G \frac{d^2\tilde{u}_G}{d\tilde{y}_G^2} \Big|_{\tilde{y}_G=-1} \right) \right] = 0, \quad (A9b)$$

$$\tilde{k} [(i\tilde{u}_L \tilde{u}_L|_{\tilde{y}_L=+1} - (i\tilde{u}_G \tilde{u}_G|_{\tilde{y}_G=-1}) \\ + \left[\left(4\tilde{v}_L \frac{d\tilde{u}_L}{d\tilde{y}_L} - i\tilde{\omega} \tilde{u}_L \Big|_{\tilde{y}_L=+1} - \left(\frac{4}{2W/H-1} \tilde{v}_G \frac{d\tilde{u}_G}{d\tilde{y}_G} - i\tilde{\omega} \tilde{u}_G \Big|_{\tilde{y}_G=-1} \right) \right] = 0 \quad (A9c)$$

and

$$[(\tilde{v}_L|_{\tilde{y}_L=+1} - (\tilde{v}_G|_{\tilde{y}_G=-1})] = 0. \quad (A9d)$$

The Chebyshev spectral method involves expanding the non-dimensional velocities and pressure using Chebyshev polynomials as follows:

$$\tilde{u}_q = \sum_{j=1}^{N+1} a_{u,j-1}^q T_{j-1}(\tilde{y}_q) = \mathbf{D}_{0,q}^{(N+1) \times (N+1)} \cdot \mathbf{a}_u^{q,(N+1) \times 1}, \quad (A10a)$$

$$\tilde{v}_q = \sum_{j=1}^{N+1} a_{v,j-1}^q T_{j-1}(\tilde{y}_q) = \mathbf{D}_{0,q}^{(N+1) \times (N+1)} \cdot \mathbf{a}_v^{q,(N+1) \times 1} \quad (A10b)$$

and

$$\tilde{p}_q = \sum_{j=1}^N a_{p,j-1}^q T_{j-1}(\tilde{y}_q) = \mathbf{D}_{0,q}^{(N+1) \times N} \cdot \mathbf{a}_p^{q,N \times 1}, \quad (A10c)$$

where T_{j-1} (Boyd 2001, p. 111) are the Chebyshev polynomials, and a_{j-1} are the corresponding coefficients in the expansion. In the matrix representation, $\mathbf{D}_{0,q}^{(N+1) \times (N+1)}$ is the matrix containing the Chebyshev polynomials, and $\mathbf{a}_u^{q,(N+1) \times 1}$ is the vector with coefficients in the expansion.

Similarly, the derivatives of the perturbations can be represented using matrix form. An example for \tilde{u}_q is

$$\left(\frac{d^k \tilde{u}_q}{d\tilde{y}_q^k} \right)^{(N+1) \times (N+1)} = D_{k,q}^{(N+1) \times (N+1)} \cdot a_u^{q, (N+1) \times 1}. \quad (\text{A11})$$

The representations of perturbations given above are substituted in the liquid and gas phase governing equations (A6) and (A7) along with the boundary conditions (A8) and interfacial conditions (A9), which are solved at the G–L points. This process results in a nonlinear eigenvalue problem, which is expressed by

$$\tilde{k}^2 C_2 \cdot a + \tilde{k} C_1 \cdot a + C_0 \cdot a = 0. \quad (\text{A12})$$

Here, \tilde{k} is the eigenvalue, and $a = [a_u^L, a_v^L, a_p^L, a_u^G, a_v^G, a_p^G]^T$ is the eigenvector involving coefficients of the Chebyshev expansion given by (A10), and C_0, C_1, C_2 are the coefficient matrices. The nonlinear eigenvalue problem given by (A12) is linearized using the matrix companion method (Bridges & Morris 1984), resulting in (2.18). This eigenvalue problem is solved using the QZ routine of the LAPACK library to obtain the complex wavenumber and the corresponding eigenfunctions, which represent the perturbation field.

REFERENCES

- AGARWAL, A., ANANTH, M. & TRUJILLO, M.F. 2022 Evaluation and improvements to interfacial curvature predictions in interFoam. *Fluids* **7** (4), 128.
- ALTIMIRA, M., RIVAS, A., RAMOS, J.C. & ANTON, R. 2010 Linear spatial instability of viscous flow of a liquid sheet through gas. *Phys. Fluids* **22** (7), 074103.
- BOECK, T. & ZALESKI, S. 2005 Viscous versus inviscid instability of two-phase mixing layers with continuous velocity profile. *Phys. Fluids* **17** (3), 032106.
- BOOMKAMP, P.A.M. & MIESEN, R.H.M. 1996 Classification of instabilities in parallel two-phase flow. *Intl J. Multiphase Flow* **22**, 67–88.
- BOYD, J.P. 2001 *Chebyshev and Fourier Spectral Methods*. Courier Corporation.
- BRACKBILL, J.U., KOTHE, D.B. & ZEMACH, C. 1992 A continuum method for modeling surface tension. *J. Comput. Phys.* **100** (2), 335–354.
- BRIDGES, T.J. & MORRIS, P.J. 1984 Differential eigenvalue problems in which the parameter appears nonlinearly. *J. Comput. Phys.* **55** (3), 437–460.
- CRAPPER, G.D., DOMBROWSKI, N. & PYOTT, G.A.D. 1975 Large amplitude Kelvin–Helmholtz waves on thin liquid sheets. *Proc. R. Soc. Lond. A.* **342** (1629), 209–224.
- CRIMINALE, W.O., JACKSON, T.L. & JOSLIN, R.D. 2019 *Theory and Computation in Hydrodynamic Stability*, 2nd edn. Cambridge University Press.
- DE LUCA, L. & COSTA, M. 1997 Instability of a spatially developing liquid sheet. *J. Fluid Mech.* **331**, 127–144.
- DELON, A., CARTELLIER, A. & MATAS, J.-P. 2018 Flapping instability of a liquid jet. *Phys. Rev. Fluids* **3** (4), 043901.
- DESHPANDE, S.S., ANUMOLU, L. & TRUJILLO, M.F. 2012 Evaluating the performance of the two-phase flow solver interFoam. *Comput. Sci. Disc.* **5** (1), 014016.
- DESHPANDE, S.S., GURJAR, S.R. & TRUJILLO, M.F. 2015 A computational study of an atomizing liquid sheet. *Phys. Fluids* **27** (8), 082108.
- DOMBROWSKI, N. & JOHNS, W.R. 1963 The aerodynamic instability and disintegration of viscous liquid sheets. *Chem. Engng Sci.* **18** (3), 203–214.
- DRAZIN, P.G. & REID, W.H. 1981 *Hydrodynamic Stability*. Cambridge University Press.

Breakup of planar liquid sheets

- FOLKSON, R. (Ed.) 2014 *Alternative Fuels and Advanced Vehicle Technologies for Improved Environmental Performance: Towards Zero Carbon Transportation*, Woodhead Publishing Series in Energy, vol. 1. Woodhead Publishing.
- FUSTER, D., MATAS, J.-P., MARTY, S., POPINET, S., HOEPPFNER, J., CARTELLIER, A.H. & Zaleski, S. 2013 Instability regimes in the primary breakup region of planar coflowing sheets. *J. Fluid Mech.* **736**, 150–176.
- HAGERTY, W.W. & SHEA, J.F. 1955 A study of the stability of plane fluid sheets. *J. Appl. Mech.* **22** (4), 509–514.
- HOYT, J.W. & TAYLOR, J.J. 1977 Waves on water jets. *J. Fluid Mech.* **83** (1), 119–127.
- JARRAHBASHI, D. & SIRIGNANO, W.A. 2014 Vorticity dynamics for transient high-pressure liquid injection. *Phys. Fluids* **26**, 101304.
- JIANG, D. & LING, Y. 2020 Destabilization of a planar liquid stream by a co-flowing turbulent gas stream. *Intl J. Multiphase Flow* **122**, 103121.
- JIANG, D. & LING, Y. 2021 Impact of inlet gas turbulence on the formation, development and breakup of interfacial waves in a two-phase mixing layer. *J. Fluid Mech.* **921**, A15.
- JUNIPER, M.P. 2007 The full impulse response of two-dimensional jet/wake flows and implications for confinement. *J. Fluid Mech.* **590**, 163–185.
- KUMAR, A. & SAHU, S. 2019 Large scale instabilities in coaxial air–water jets with annular air swirl. *Phys. Fluids* **31** (12), 124103.
- LEFEBVRE, A.H. & MCDONELL, V.G. 2017 *Atomization and Sprays*, 2nd edn. CRC.
- LI, X. 1993 Spatial instability of plane liquid sheets. *Chem. Engng Sci.* **48** (16), 2973–2981.
- LI, X. & TANKIN, R.S. 1991 On the temporal instability of a two-dimensional viscous liquid sheet. *J. Fluid Mech.* **226**, 425–443.
- MARMOTTANT, P. & VILLERMAUX, E. 2004 On spray formation. *J. Fluid Mech.* **498**, 73–111.
- MATAS, J.-P. & CARTELLIER, A. 2013 Flapping instability of a liquid jet. *C. R. Méc* **341** (1–2), 35–43.
- MATAS, J.-P., DELON, A. & CARTELLIER, A. 2018 Shear instability of an axisymmetric air–water coaxial jet. *J. Fluid Mech.* **843**, 575–600.
- OBERLEITHNER, K., RUKES, L. & SORIA, J. 2014 Mean flow stability analysis of oscillating jet experiments. *J. Fluid Mech.* **757**, 1–32.
- ODIER, N., BALARAC, G. & CORRE, C. 2018 Numerical analysis of the flapping mechanism for a two-phase coaxial jet. *Intl J. Multiphase Flow* **106**, 164–178.
- ODIER, N., BALARAC, G., CORRE, C. & MOUREAU, V. 2015 Numerical study of a flapping liquid sheet sheared by a high-speed stream. *Intl J. Multiphase Flow* **77**, 196–208.
- POPE, S.B. 2000 *Turbulent Flows*. Cambridge University Press.
- RANGEL, R.H. & SIRIGNANO, W.A. 1991 The linear and nonlinear shear instability of a fluid sheet. *Phys. Fluids A* **3** (10), 2392–2400.
- RUSCHE, H. 2003 Computational fluid dynamics of dispersed two-phase flows at high phase fractions. PhD dissertation, Imperial College London (University of London).
- SCHMID, P.J. & HENNINGSON, D.S. 2000 *Stability and Transition in Shear Flows*. Springer.
- SCHMIDT, S. & OBERLEITHNER, K. 2020 Instability of forced planar liquid jets: mean field analysis and nonlinear simulation. *J. Fluid Mech.* **883**, A7.
- SINGH, G., KOURMATZIS, A., GUTTERIDGE, A. & MASRI, A.R. 2020 Instability growth and fragment formation in air assisted atomization. *J. Fluid Mech.* **892**, A29.
- SQUIRE, H.B. 1953 Investigation of the instability of a moving liquid film. *Brit. J. Appl. Phys.* **4** (6), 167–169.
- TAMMISOLA, O., SASAKI, A., LUNDELL, F., MATSUBARA, M. & SÖDERBERG, L.D. 2011 Stabilizing effect of surrounding gas flow on a plane liquid sheet. *J. Fluid Mech.* **672** (672), 5–32.
- TENG, C.H., LIN, S.P. & CHEN, J.N. 1997 Absolute and convective instability of a viscous liquid curtain in a viscous gas. *J. Fluid Mech.* **332**, 105–120.
- TRYGGVASON, G., SCARDOVELLI, R. & ZALESKI, S. 2011 *Direct Numerical Simulations of Gas–Liquid Multiphase Flows*. Cambridge University Press.
- TURNER, M.R., HEALEY, J.J., SAZHIN, S.S. & PIAZZESI, R. 2011 Stability analysis and break-up length calculations for steady planar liquid jets. *J. Fluid Mech.* **668**, 384–411.
- UBBINK, O. & ISSA, R.I. 1999 A method for capturing sharp fluid interfaces on arbitrary meshes. *J. Comput. Phys.* **153** (1), 26–50.
- WANG, B., JIANG, Y., HUTCHINS, P., BADAWY, T., XU, H., ZHANG, X., RACK, A. & TAFFOREAU, P. 2017 Numerical analysis of deposit effect on nozzle flow and spray characteristics of GDI injectors. *Appl. Energy* **204**, 1215–1224.
- WU, P.K. & FAETH, G.M. 1995 Onset and end of drop formation along the surface of turbulent liquid jets in still gases. *Phys. Fluids* **7** (2915), 2915–2917.

- YECKO, P., ZALESKI, S. & FULLANA, J.-M. 2002 Viscous modes in two-phase mixing layers. *Phys. Fluids* **14** (12), 4115–4122.
- ZANDIAN, A., SIRIGNANO, W.A. & HUSSAIN, F. 2017 Planar liquid jet: early deformation and atomization cascades. *Phys. Fluids* **29** (062109), 1–20.